Master's Thesis in Marine
Biogeochemistry

Anthropogenic Carbon in the Nordic seas and Arctic Ocean, 1994 to 2007

Anne Kari Øhman Meisingset

University of Bergen
Geophysical Institute

June 3, 2019

Abstract

The increase of anthropogenic CO_2 between 1994 and 2007, ΔC_{ant}, is quantified in the Nordic seas and Arctic Ocean with the extended multiple linear regression method (eMLR(C*)). To be able to map the increase in C_{ant} with the eMLR(C*) method in all parts of the Nordic seas and the Arctic Ocean, climatological distribution for the seven variables; temperature, salinity, alkalinity, AOU, nitrate, phosphate, and silicate, have been prepared. Anthropogenic carbon concentrations in the Nordic seas have increased by between 5.0 and 11.1 μmol/kg between 1994 and 2007. The increase in column inventories of ΔC_{ant} in the Nordic seas were $\sim$15 - 25 moles/m^2, with the largest increase in the Lofoten Basin. The results for the Nordic Seas agree in general with previous studies. However, in the Greenland Sea, the increase of C_{ant} is a bit lower than expected. This may be a result of increasing deep mixing that brings old water masses, with relatively low concentrations of C_{ant}, to the upper ocean. The Arctic Ocean has the highest estimates of ΔC_{ant}, both for column inventories and individual water masses. Some parts of the Eurasian Basin have a column inventory of ΔC_{ant} of $\sim$30 moles/m^2, associated with a very large increase in C_{ant} for some of the water masses. These high values are likely unrealistic and related to variability in data coverage and water mass distributions, as well as to deficiencies in the water mass definition schemes themselves.

Acknowledgements

I would like to thank my brilliant supervisors, Are Olsen, Truls Johannessen, and Morven Muilwijk, for the guidance and support along the way. I am grateful for having supervisors that always keep an open door if I need someone to discuss my problems (mostly thesis related) with. Also, a big thanks to my father for giving me the opportunity to use GeoCap, and for being very patient when helping me create the climatologies in a few long and hectic days in Oslo. Thanks to Odd for creating a memorable year, and for joining me in setting a new record in coffee drinking and long nights at the office. A very big thank you to my partner, Erlend, for inspiring, motivating, and supporting me through the last ten months. Last, thanks to GFI and all the people I have met here, both students and employees, during my three years in Bergen. It has been three challenging, interesting, and fun years.

List of abbreviations

C_{ant} - Anthropogenic CO_2
DIC - dissolved inorganic carbon
Rf - Revelle factor
Alk - Total alkalinity
EB - Eurasian Basin
CB - Canadian Basin
GSR - Greenland-Scotland Ridge
AOU - Apparent oxygen utilization
TSS - Transient Steady State
MLR - multiple linear regression
eMLR - extended multiple linear regression
RMSE - root-mean-square-error
WOA - World Ocean Atlas
C_{ant} - Anthropogenic CO_2
AO - Arctic Ocean
NS - Nordic seas

Water masses

PW1 - Polar Water 1
PW2 - Polar Water 2
AAW - Arctic Atlantic Water
DAAW - Dense Arctic Atlantic Water
uPDW EB - upper Polar Deep Water for the Eurasian Basin
uPDW CB - upper Polar Deep Water for the Canadian Basin
AW - Atlantic Water
DAW - Dense Atlantic Water
AIW - Arctic Intermediate Water
EBDW - Eurasian Basin Deep Water
CBDW - Canadian Basin Deep Water
NDW - Nordic seas Deep Water
GSDW - Greenland Sea Deep Water

Contents

Chapter 1

Introduction

Since the beginning of the industrial revolution, CO_2 corresponding to ∼640 Gt of CO_2 has been emitted to the atmosphere by fossil fuel combustion, cement production, and land use change. 270 Gt has stayed in the atmosphere, causing the CO_2 concentration to rise from 280 ppm in preindustrial times, to 410 ppm in 2018, while the rest has been absorbed by the oceans and terrestrial biosphere.

The ocean has been the only true net sink of anthropogenic CO_2 in the past 200 years, and its ability to absorb and store CO_2 plays an essential role for the Earth's climate. According to today's estimates, the ocean stores between 25 and 30 percent of all anthropogenic CO_2 emitted annually (Le Quéré et al., 2018; Gruber et al., 2018). As anthropogenic CO_2 levels rise in the atmosphere, the ocean will keep storing CO_2. Sabine et al. (2004) estimated that by 1994, the ocean had stored 50% of all CO_2 emitted by humans since the industrial revolution, but that the potential is much larger on longer time scales. One rotation of the conveyor belt takes about 1000 years, and the ocean needs several rotations to fully equilibrate with the atmospheric. Over a few millennia, about 80% of the total anthropogenic CO_2 can be taken up by the oceans (Sabine et al., 2004). If we let the system fully equilibrate with the seafloor sediments, silicate rock weathering, and river input, all of the anthropogenic CO_2 in today's atmosphere can be stored in the ocean (Sarmiento and Gruber, 2006).

Models show that the ocean's uptake efficiency likely will decline in the future (Friedlingstein et al., 2006; Schwinger et al., 2014). Accordingly, the reduction is primarily a result of decreasing overturning circulation, as the upper ocean gets more stratified because of climate change. The upper ocean has little storage capacity because of its small volume (Sarmiento et al., 1992). Therefore, it is the transport from the surface to the deep that is the rate-limiting step for anthropogenic CO_2 uptake in the ocean. By continuously monitoring the ocean sink, we can keep track of how it changes. This knowledge provides insight on its climate change sensitivity and the redistribution of emitted CO_2 in the global carbon cycle.

Gruber et al. (2018) used the eMLR(C*) method (Clement and Gruber, 2018) to estimate the global uptake and inventory of anthropogenic CO_2 (C_{ant}) from 1994 to 2007. They compared data from the WOCE/JGOFS era in the 1990s to data from the Repeat Hydrography/GO-SHIP period in the 2000s, and estimated the change in C_{ant}, ΔC_{ant}, based on a linear regression model. They estimated an increase in the global ocean inventory of 33±4 Pg carbon between 1994 and 2007.

Their study showed that the highest uptake was in the North and South Atlantic, while the lowest was in the the upwelling zones. The total uptake was as expected compared to the atmospheric increase in this period, and the global distribution matched with the uptake pattern in Sabine et al. (2004) (see Figure 2.3). However, there are some differences in the Atlantic Ocean, most likely arising from circulation changes (Gruber et al., 2018). The uptake represents 30±4% of the global emissions, which is the same percentage as Sabine et al. found in 2004.

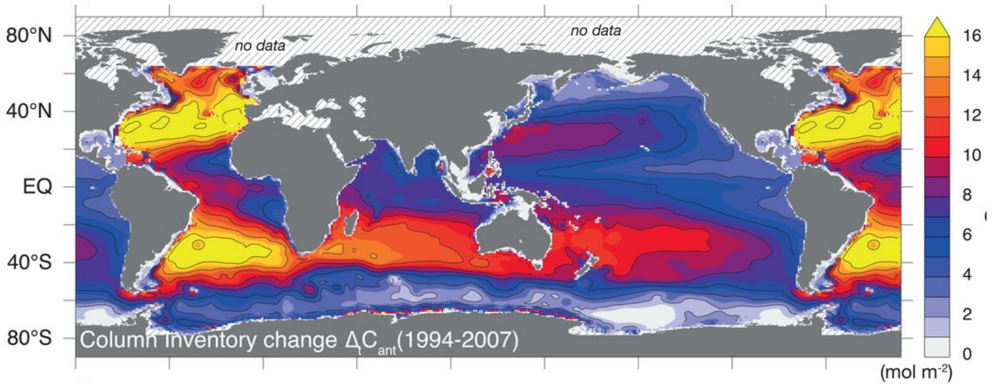

Figure 1.1: Global C_{ant} inventory estimated with the eMLR(C*) method. The Arctic Ocean and Nordic seas are left out (Gruber et al., 2018).

Unfortunately, Gruber et al. (2018) excluded the Nordic Seas and Arctic Ocean from their eMLR(C*) analysis, as can be seen from Figure 1.1. Instead, they added the results of Olsen et al. (2010) and Tanhua et al. (2009) to the total uptake. The complexity and poor data coverage in the Nordic seas and Arctic Ocean make it difficult to implement the eMLR(C*) method since it relies on steady-state circulation and well-defined climatologies. Neither of these exists in this region. In addition, Gruber et al. (2018) used isopycnal slabs to separate between the eMLR(C*) equations. The ocean density is too homogenous in the Arctic Ocean and Nordic seas to use isopycnal slabs for water mass division. There are also relatively little data from the 90s, especially when considering the great variability.

While the Arctic Ocean and Nordic seas are small in size compared to the global oceans, they have great potential for storing C_{ant} due to extensive ventilation. In the Nordic seas, open ocean convection in the Greenland and Iceland gyre and recirculated Atlantic Water contribute to the formation of newly ventilated deep water (Brakstad et al., 2019). From the Arctic Ocean, Atlantic and Intermediate Water, which are both high in C_{ant} (Tanhua et al., 2009), exit through the Fram Strait and into the Nordic seas. These processes link the Arctic Ocean and Nordic seas to the global carbon system as the dense water masses rich in C_{ant} flow southward over the Greenland-Scotland Ridge and enter the North Atlantic (Mauritzen, 1996). This newly ventilated water causes the deepest intrusion of C_{ant} in the world, resulting in a column inventory change of $\sim$16 mol C/m^2 between 1994 and 2007 in the mid-latitude North Atlantic - twice the global mean storage rate per year (Gruber et al., 2018).

In this thesis, I will use the eMLR(C*) method in the Nordic seas and the Arctic Ocean to estimate C_{ant} uptake and storage in the same period of time as Gruber et al. (2018). I will use data from GLODAPv2 (Olsen et al., 2016), in addition to data from more recent cruises, and address the problems mentioned above. This entails overcoming future challenges like making new climatologies and use water mass definitions from Rudels et al. (2012) instead of isopycnal slabs.

Chapter 2

Theoretical background

2.1 Seawater CO_2-chemistry and anthropogenic carbon

The CO_2 chemistry in seawater is governed by the following three equilibrium reactions:

1)

$$CO_{2,gas} + H_2O \rightleftharpoons H_2CO_3^* \tag{2.1}$$

2)

$$H_2CO_3^* \rightleftharpoons HCO_3^- + H^+ \tag{2.2}$$

3)

$$HCO_3^- \rightleftharpoons CO_3^{2-} + H^+ \tag{2.3}$$

There are in total three different carbon species involved in the equilibria. The concentration of all of them combined equals the dissolved inorganic carbon (DIC):

$$DIC = [H_2CO_3^*] + [HCO_3^-] + [CO_3^{2-}] \tag{2.4}$$

When CO_2 dissolves, it reacts with the water and forms carbonic acid, but it is difficult to distinguish between the two. Therefore, $H_2CO_3^*$ is the sum of dissolved CO_2 and carbonic acid, H_2CO_3.

The distribution of the three species in Equation 2.4 is linked to the pH of the ocean. This dependency can be visualized through a Bjerrum plot (Figure 2.1).

A very special feature of the ocean is that, on average, only one in twenty CO_2 molecules react with water and form carbonic acid according to Equation 2.1. This is because seawater contains large amounts of carbonate, CO_3^{2-}, from weathering of volcanic siliceous rocks:

$$CaSiO_3 + CO_2 = SiO_2 + Ca^{2+} + CO_3^{2-} \tag{2.5}$$

Thus, the most important reaction in the ocean when it comes to uptake of anthropogenic carbon is the reaction between these carbonate ions and CO_2. On average, the oceanic uptake of 19/20 CO_2 molecules from the atmosphere follows the following equation (Sarmiento and Gruber, 2006):

$$CO_2 + H_2O + CO_3^{2-} \rightleftharpoons 2HCO_3^-, \tag{2.6}$$

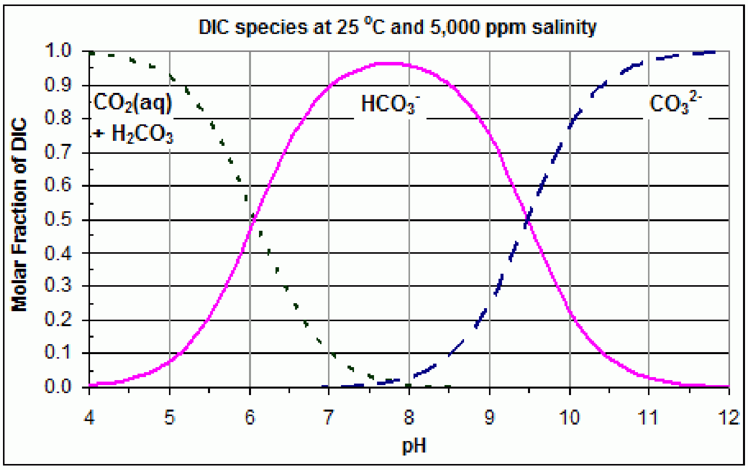

Figure 2.1: Bjerrum plot; relationship between pH and the different inorganic carbon species *(https://en.wikipedia.org/wiki/Revelle_factor)*.

where the strongest base in the ocean, CO_3^{2-}, reacts with the strongest acid, $H_2CO_3^*$, and forms bicarbonate, HCO_3^-. In this way, the carbonate ions are buffering the ocean since it neutralizes the dissolved CO_2.

If it were not for the presence of carbonate ions in the ocean, the uptake of CO_2 would act as any other gas, i.e every molecule of absorbed CO_2 would have increased the ocean's back-pressure accordingly, and the uptake would quickly come to a stop.

2.2 Ocean uptake of anthropogenic CO_2

We consider the uptake of natural CO_2 and anthropogenic CO_2 as two different processes, even though they are the same molecule. The anthropogenic uptake can be seen as an "extra" signal of DIC on top of the natural steady state processes operating in the background ocean.

The uptake of natural CO_2 in the surface ocean is dependent on the solubility pump, soft tissue pump, and carbonate pump, while the uptake of C_{ant} into the surface ocean is strongly dependent on the *Revelle factor* (Maier-Reimer and Hasselmann, 1987). The soft tissue pump and carbonate pump are biological processes, and will not change when extra CO_2 is added to the ocean. Biology is limited by nutrients, light, and vertical mixing, not by the concentration of CO_2 (Sarmiento and Gruber, 2006). Therefore, C_{ant} can be treated as a passive tracer moving with the ocean circulation. Natural DIC will, on the other hand, increase due to remineralization of organic matter after the water has left the surface. This is why DIC increases in old deep water masses.

Essentially, the Revelle factor determines the C_{ant} solubility in the surface ocean. The Revelle factor quantifies the ocean's ability to buffer uptake of CO_2 as the atmospheric content increases, with values that typically range between 8 and 13. A low Revelle factor is proportional to a large buffer capacity, while a high factor means that the buffer capacity is low and the ocean is more *sensitive* to an increase of CO_2. In this case, less than 19/20 of CO_2 molecules will react with carbonate and form bicarbonate (Equation 2.6), and more CO_2 will remain as such and increase the ocean's CO_2 back-pressure to the atmosphere. I.e., when the concentration of dissolved CO_2 increases, the partial pressure difference between the atmosphere and the ocean decreases, and the uptake potential of C_{ant} reduces. On the other hand, high buffer capacity is proportional to a smaller change in the dissolved CO_2 concentration, since there are better availability of carbonate ions. More than 19/20 of the molecules react with carbonate in these areas. In general, the same increase in CO_2 will lead to a larger change in pH in an area with low buffer capacity compared to an area with high buffer capacity. The availability of carbonate ions is the most important factor (see Equation 2.8 and 2.9).

The Revelle factor is defined as the instantaneous change in pCO_2 over the instantaneous change in DIC:

$$Rf = \frac{\Delta pCO_2/pCO_2}{\Delta DIC/DIC}, \tag{2.7}$$

where ΔpCO_2 is the change in pCO_2. pCO_2 and DIC are the mean values in the water mass. The Revelle factor can also be approximated as:

$$Rf \approx \frac{2 \cdot DIC - 3 \cdot Alk}{((Alk/DIC) - 2) \cdot (Alk - DIC)}, \tag{2.8}$$

and carbonate can be approximated as the difference between total alkalinity (Alk) and DIC (Sarmiento and Gruber, 2006):

$$[CO_3^{2-}] \approx Alk - DIC \tag{2.9}$$

As seen from Equation 2.8, the Revelle factor is dependent on the relationship between DIC and Alk. Similarly, the concentration of carbonate, which regulates the buffer capacity, can be approximated as the surplus of Alk over DIC (Equation 2.9). If DIC increases, the Revelle factor increases, and the buffer capacity decreases. If the alkalinity increases, consequently the Revelle factor decreases, and the buffer capacity increases. In other words, the greater the ratio [Alk]/[DIC], the more C_{ant} can be taken up at the surface as the surplus of CO_3^{2-} is larger. Figure 2.1 illustrates how an increase in the concentration of dissolved CO_2 reduces the pH and buffer capacity since the carbonate concentration decreases.

Figures 2.2 illustrates the geographical distribution of the Revelle factor. High values are typically found in high latitude waters; these areas have a low buffer capacity and low C_{ant} solubility. This is a bit surprising since CO_2 is more soluble in cold water than in warm. However, C_{ant} solubility is only dependent on the DIC/Alk ratio. Cold water holds more DIC and dissolved CO_2 than warm water, and the carbonate ions have been used by the the absorption of this DIC. This results in a high DIC/Alk ratio and a low buffer capacity. There are differences between the North Pacific and North Atlantic even though they are at the same latitude. Upwelling in the North Pacific brings up water with relatively high nutrient and DIC concentration. The biology is not able to utilize all the available macronutrients in these areas, resulting in a higher DIC/Alk ratio than in the North Atlantic. This is also the case for the Southern Ocean, where the lowest values are found in the warm, stable, subtropical areas. Here, the waters are warm and biological production has used most of the macronutrients in the surface layer, including DIC, leading to a low DIC/Alk ratio (Egleston et al., 2010).

Figure 1.1 and 2.3 show the C_{ant} column inventory. Comparing Figure 2.2 with the inventory, it is clear that the Revelle factor in the surface layer and the column inventory of C_{ant} do not match.

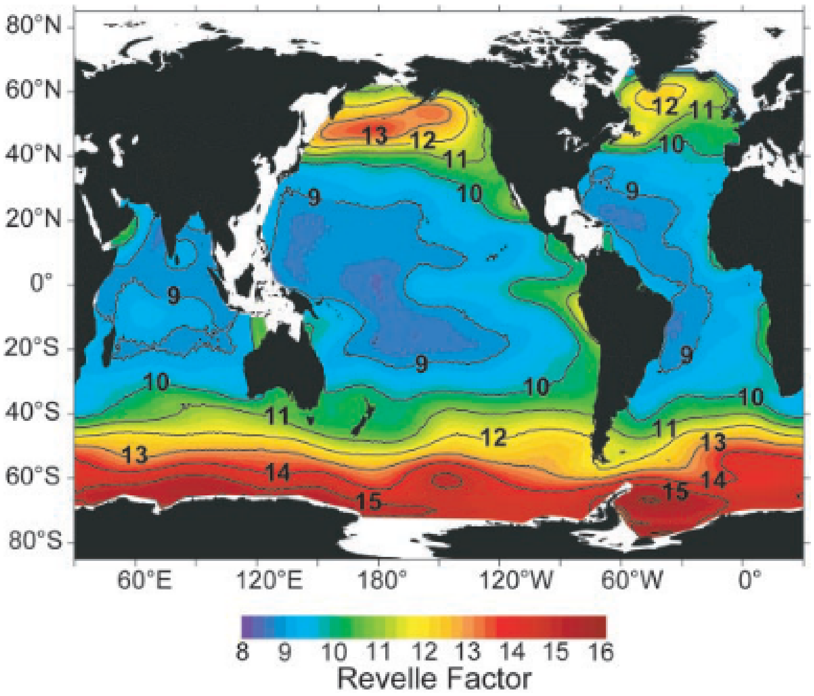

Figure 2.2: Geographical distribution of the Revelle factor averaged for the upper 50 meters, inversely proportional to the uptake potential of CO_2 at the surface. (Sabine et al., 2004)

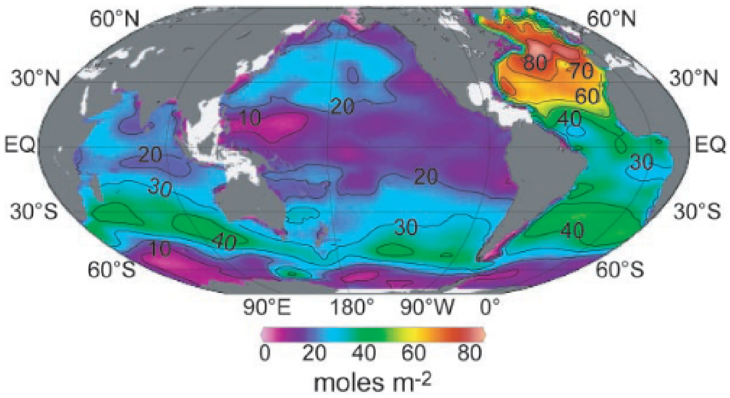

Figure 2.3: Geographical distribution of the column inventory of C_{ant} in 2004 (Sabine et al., 2004).

When the amount of CO_2 increases in the atmosphere, the ocean will absorb CO_2 until the air and surface ocean reach a new state of equilibrium. This uptake is governed by the Revelle factor. If the surface ocean was motionless, a new equilibrium state would be reached after one year. After that, surface water needs to be replaced to continue absorbing CO_2. In some parts of the Nordic seas and the Arctic Ocean, this replacement happens very efficiently because of the intense ventilation in these regions. Even if the Revelle factor is high here, the vertical transport of water brings C_{ant} deep into the interior. In contrast, the North Pacific lacks ventilation, leading to low column inventories. The northern parts of the Southern Ocean have a relativity large inventory due to the ventilation of the Antarctic Mode Water and the Antarctic Intermediate Water.

2.3 The Arctic Ocean and Nordic seas

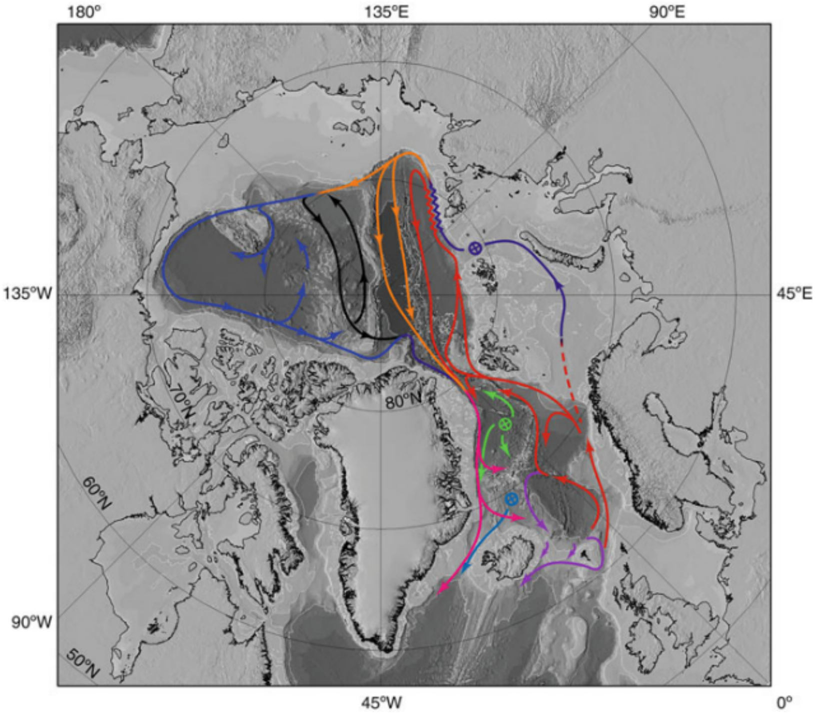

Figure 2.4: Main circulation pattern in subsurface and intermediate layers, from Rudels et al. (2012). Circles with crosses are areas with possible deep convection.

The Arctic Ocean and Nordic seas consist of several deep basins that are connected through the Fram Strait and the Barents Sea. In the Arctic Ocean, there are two large basins separated by the Lomonosov Ridge; the Eurasian Basin (EB) and the Canadian Basin (CB). They are ∼5500 and ∼4000 meters at their deepest. In addition to the connection with the Nordic seas, there are two more gateways to the world oceans; the Bering Strait and the Canadian Archipelago.

The Nordic seas consists of the relatively deep Norwegian Basin, the Lofoten Basin, and the Greenland basin, in addition to the shallower Iceland Sea. The deep basins reach depths of almost 4000 meters. The Nordic seas are separated from the North Atlantic in the south by the Greenland-Scotland Ridge (GSR). The deepest part of the GSR is the Faroe Bank Channel at ∼850 meters. Here, and through the Denmark Strait, relatively deep and dense water exits and enters the Atlantic Ocean, while the deepest and densest water is trapped inside the basins.

The Nordic seas are dominated by inflowing Atlantic Water in the east, and outflowing Polar Water in the west, shown by the red and pink arrows in Figure 2.4. Polar Water and Atlantic Water mix in the middle of the Nordic seas and create Arctic Surface Water. These three water masses represent the upper layers of the Nordic seas. The intermediate layer forms when Arctic Surface Water sinks and becomes Arctic Intermediate Water. The deep water in the Nordic seas is formed locally through deep mixing in the Greenland Basin, among other places, and through advection from the Arctic Ocean via the Fram Straight (Bluhm et al., 2015).

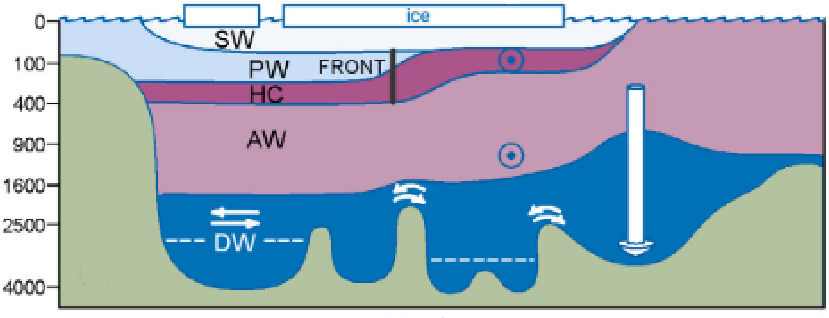

Figure 2.5: Main Arctic Ocean water masses. Pacific Water (PW) and halocline (HC) make up the halocline described in the text. SW = Surface Water, AW = Atlantic Water, and DW = Deep Water. From Bluhm et al. (2015). The basin to the right is the Greenland Basin with a tube representing bottom water formation. The figure is somewhat outdated, since there have not been bottom water formation in the Greenland Sea since the early 80's.

The Arctic Ocean consists of four main layers: the Surface Water, the halocline, the Atlantic Water, and the Deep Water. The surface water consists of Atlantic and Pacific origin water, river input, sea ice melt, and precipitation (Yamamoto-Kawai et al., 2009). The halocline is mainly made up of shelf water (Bluhm et al., 2015), and consist of modified water originating from both the Atlantic and the Pacific. The Atlantic layer consists of the warm and high salinity modified Atlantic water. The deep water is partly formed locally by brine rejection on the shelves and partly from deep waters that flow in from the Norwegian Sea. The deepest water in the CB is about 450 years old, while the deepest water in the Eurasian Basin is about 250 (Bluhm et al., 2015).

In the Arctic Ocean, the circulation broadly follows the topographic features in a cyclonic manner. Atlantic water flows through the Nordic seas and enters the Arctic Ocean through the Fram Strait and the Barents Sea. The Fram Strait branch flows into the EB where it gets covered by freshwater and ice, north of Svalbard. The Barents Sea branch cools and sinks down the St. Anna Trough, as shown by the purple arrow in Figure 2.4. These two branches are of similar size and meet in the EB north of Kara Sea (Rudels et al., 2012). From here, they circulate cyclonically before exiting through the Fram Strait (Mauritzen, 1996). This is the only place where deep water exchange in or out from the Arctic Ocean happens. Apart from this exchange, the deep water is trapped inside the basins. The surface circulation (not illustrated in 2.4) consists mainly of shallow inflow from the Pacific Ocean and riverine input. Most of the surface water exits along the east coast of Greenland via the East Greenland Current, while some of it exits through the Canadian Archipelago (Rudels et al., 2012).

The ventilation of the Arctic Ocean happens through inflowing Atlantic Water and brine rejection. The Atlantic Water has been in contact with the atmosphere for many years before it enters the Arctic Ocean where it subducts and circulates under the surface layer. This input leads to a substantial renewal of subsurface and intermediate water. When it comes to brine, it is produced during winter when seawater freezes and rejects high salinity water to the underlying ocean. The main production areas are on the shelves. The brine plumes typically sink down the continental slope and spread into the basins. However, their ventilation properties are not well described in literature.

Chapter 3

Data and Methods

3.1 Data

The data used in this theses are divided into two parts: data for making the eMLR(C*) equations, and data for making the climatologies. To make the eMLR(C*) equations, every sample has to contain eight variables. That is temperature, salinity, total alkalinity, apparent oxygen utilization (AOU), nitrate, phosphate, silicate, and total carbon. This is not necessary for the climatologies, since they are made independently for each variable.

3.1.1 Data for the eMLR(C*) equations

The data used to produce the eMLR(C*) equations are mainly from the **GLODAP version 2 data product (Olsen et al., 2016)**. In addition, I added data from five more recent cruises from the Arctic Ocean. These are:

* R/V Polarstern, cruise: TransArc, 2011, Central Arctic (Anderson et al., 2011)
* R/V Polarstern, cruise: TransArc II, 2015, Arctic Ocean - Eurasian Basin (Jones and Ulfsbo, 2017)
* R/V Helmer Hansen, cruise: EXPOCODE: 58HJ20120807, 2012, Arctic Ocean - north of Svalbard
* R/V Oden, cruise: LOMROG, 2007, Lomonosov Ridge of Greenland (Polarforskningssekretariatet, 2017)
* HEALY, cruise: HLY1502, 2015, Arctic Ocean - Canadian Basin *https://cchdo.ucsd.edu/cruise/33HQ20150809*

Before creating the final data set from which I make the eMLR(C*) equations, the data were subjected to quality control and further and processing.

Data processing:

* Remove outliers, NaNs, and bad quality data.
* Calculate potential temperature with the ”seawater” package for all samples missing it.

- Calculate AOU for the added cruises with the equations from Garcia and Gordon (1992). This is how AOU is computed in GLODAP version 2 as well.
- Calculate potential density with the seawater package.
- Calculate total alkalinity with CO2SYS whenever both DIC and pH were available, and measured Alk not.
- Remove all samples that does not contain all eight variables mentioned above.
- Convert nutrient data to μmol/kg.

3.1.2 Data for the climatologies

In addition to the data used to make the eMLR(C*) equations, I added salinity and temperature data from the UDASH database (Behrendt et al., 2018) and nutrient data from the North Atlantic and Nordic Seas hydrography collection (NANSHY) .

Data processing:

- Remove all data below 55 degrees latitude.
- Remove data from the Pacific Ocean, Labrador Sea, and the coast of Norway.
- Remove winter data (October - April) from the upper 200 meters to avoid and exclude the seasonal changes caused by the winter mixed layer.
- Remove outliers, NaNs, and bad quality data.
- Convert nutrient data to μmol/kg.

3.2 Methods

To find the change of C_{ant} in the Arctic Ocean and Nordic seas t_1 = 1994 and t_2 = 2007, I use the eMLR(C*) method described by Clement and Gruber (2018). This is an improvement and combination of previous methods, namely the eMLR method of Friis et al. (2005), the C* approach of Gruber et al. (1996), and the transient steady state (TSS) method of Tanhua et al. (2007). The uncertainty in the eMLR(C*) method is reduced compared to the eMLR method of Friis et al. (2005), as I will explain later.

The change in DIC at one particular place in the ocean from t_1 to t_2, ΔDIC(t_2 - t_1), is the result of many different processes, both natural and anthropogenic. In addition to the processes described in Chapter 2, circulation and mixing can also change the DIC content. Therefore, since ΔDIC(t_2 - t_1) is a result of more than just the anthropogenic signal, we need an indirect method like eMLR(C*) to separate changes in C_{ant} from natural variations in DIC.

Wallace (1995) was the first trying to overcome the challenge of separating C_{ant} from natural CO_2 over a time period, ΔC_{ant}(t_2 - t_1), by using a multi linear regression method (MLR). The principle is then, that the bias in the estimated DIC for t_2, reflects changes in C_{ant}. He created a multiple linear regression equation for t_1 to predict the carbon in t_2. The MLR equation for

t_1 relates DIC to hydrographic and biogeochemical variables, like temperature, salinity, alkalinity, AOU, and nutrients:

$$DIC = a \cdot X_1 + b \cdot X_2 + c \cdot X_3 ...etc, \tag{3.1}$$

These variables are able to describe the distribution of DIC in the water column since they reflect the processes that governs the DIC distribution; temperature affects DIC through solubility; salinity through its definition (salinity contains both bicarbonate and carbonate); alkalinity through the Revelle factor; and nutrients and AOU through the biological production/remineralization of organic matter, which affect DIC through the stoichiometry. AOU is the "apparent oxygen utilization", defined as $O_{2,sat}$ - $O_{2,obs}$. $O_{2,sat}$ is the saturation concentration of oxygen in a water parcel, while $O_{2,obs}$ is the measured oxygen. Oxygen is used in remineralization, such that AOU increases with time after a water parcel leaves the surface.

When an MLR equation like Equation 3.1 is established for t_1, it is used on a data set from t_2. The predicted DIC, calculated from Equation 3.1, is subtracted from the observed DIC at t_2, and the difference interpreted as the change in C_{ant} from t_1 to t_2. Any natural change in DIC will be described by Equation 3.1 and accounted for. The difference between observed DIC and predicted DIC is reflecting the anthropogenic change alone as long as these assumptions are met:

1) The DIC value anywhere in a specific water mass can be described by a multi linear equation that relates DIC (response variable) to other hydrographic and biogeochemical properties (predictor variables).
2) The underlying natural correlation between DIC and predictor variables does not change during the time period t_1 to t_2.
3) The C_{ant} change is not affecting any of the predictor variables, and is only a result of the increasing CO_2 levels in the atmosphere.
4) Circulation and mixing are invariant between t_1 and t_2.

This also implies that if the correlation between DIC and the predictors variables change in time, it will result in errors in the estimated C_{ant}. A spatial change in correlation is less serious, since it will be eliminated by the MLR equations and not affect the change in C_2 between t_1 and t_2.

Based on the MLR method, Friis et al. (2005) created the "extended MLR method" (eMLR), an improvement of the earlier method as it has less error in the C_{ant} estimates. Friis et al. (2005) use two MLR equations, one for t_1 and one for t_2. The coefficients of the predictor variables in equation 1 are subtracted from those of equation 2, resulting in one single equation that estimates anthropogenic CO_2 uptake between t_1 and t_2 (Equation 3.2 - 3.4). The eMLR method is based on the same assumptions as the MLR method.

Reference year 1:

$$DIC(t_1^{ref}) = a_1 + b_1 \cdot V_1(t_1) + c_1 \cdot V_2(t_1) + ... + z_1 \cdot V_k(t_1) + Residuals(t_1), \tag{3.2}$$

Reference year 2:

$$DIC(t_2^{ref}) = a_2 + b_2 \cdot V_1(t_2) + c_2 \cdot V_2(t_2) + ... + z_2 \cdot V_k(t_2) + Residuals(t_2), \tag{3.3}$$

Combined:

$$\Delta C_{ant}^{eMLR}(t_2^{ref} - t_1^{ref}) = (a_2 - a_1) + (b_2 - b_1) \cdot V_1 + (c_2 - c_1) \cdot V_2 + ... + (z_2 - z_1) \cdot V_k + (Res(t_2) - Res(t_1)), \tag{3.4}$$

where a, b, c, and z are the regression coefficients, V_1, V_2, V_k are the predictor variables, and the subscripts 1 and 2 are the two years that are compared.

If the coefficients do not change, the resulting equation thet express the increase of C_{ant} from t_1 to t_2 (Equation 3.4) equals zero. In that case, if there *is* a change in observed DIC from t_1 to t_2 it means that this change is a result of natural variation, which the eMLR equation accounts for. If the resulting equation does not equal zero, DIC has changed compared to the other variables due to C_{ant} uptake.

The data sets from t_1 and t_2 have to originate from the same area or water mass, otherwise regional natural processes can cause errors in the C_{ant} estimates. Either the first or the second data set can be used as input when Equation 3.4 is used to determine Cant increase, but it is preferable to use the one with the highest quality data. Equation 3.4 estimates C_{ant} at the location for the input data. A problem with this method is that there are rather few places where there have been repeated cruises with measurements for all the necessary variables. This makes the method unsuited for a large portion of the global ocean.

Clement and Gruber (2018) improved the eMLR method in the following ways:
1) Instead of DIC, they use DIC corrected for biological processes, C*, as the response variable (Section 3.2.1). The oceanic variability is less for C* than for DIC, which means a regression analysis with C* as the response variable instead of DIC will tend to have smaller uncertainties. Also, ΔC* resembles the pattern of ΔC_{ant} more than ΔDIC, which also make approach less prone to errors.
2) They used the TSS assumption to normalise data from two periods/eras to two reference years, which increases the availability of data for t_1 and t_2. (Section 3.2.2).
3) Instead of only using one eMLR-equation for each region, Clement and Gruber (2018) used the results of ten equations to generate more robust C_{ant} estimates (Section 3.2.3).

This approach is called the eMLR(C*) method. I will explain this in the next sections.

3.2.1 C*

The DIC concentration in a water mass is, as mentioned, determined by many different processes, both natural and anthropogenic. If we assume that stoichiometric ratios are constant, we can take advantage of what we know about natural biological processes and remove their impact on the DIC distribution by making a new variable, C*, as described in Gruber and Sarmiento (2002).

When marine organic matter is remineralized, carbon in its inorganic form is added to the ocean. Other nutrients, like nitrate and phosphate, are added at the same time, in a ratio that is equal to the ratio in the organic matter. Redfield et al. (1963) found this relationship to be carbon:nitrate:phosphate = 106:16:1, broadly valid for the global ocean. In other words, the oceans' stoichiometry, or the Redfield ratio, is a result of remineralized organic matter. We can use the Redfield ratio together with phosphate, PO_4, to correct the DIC for carbon added by remineralization of organic matter in the water column:

$$C^* = DIC - r_{c:p} \cdot PO_4 - 0.5 \cdot (Alk + r_{n:p} \cdot PO_4). \tag{3.5}$$

$r_{c:p}$ and $r_{n:p}$ are the stoichiometric ratios between carbon, phosphate, and nitrate. If these stoichiometric ratios are correct and constant, C* removes the carbon originating from both steady and non steady state biological processes. What is left is a result of natural air-sea gas exchange and anthropogenic CO_2 uptake. However, the stoichiometric ratios are not constant throughout the world ocean (e.g., Martiny et al., 2013). They vary on both time and space. Therefore, here I use the ratios determined for the North Atlantic by Körtzinger et al. (2001), with mean values for $r_{c:p}$ and $r_{n:p}$ of 126 and 17.5, respectively.

The last term on the right side of Equation 3.5 corrects for the dissolution of $CaCO_3$ shells and skeletons of marine calcifying organisms. This releases CO_3^{2-} ions into the water, which will lead to an increase in Alk. The effect on DIC is 0.5 times the effect on Alk as carbonate ions contribute twice to Alk:

$$Alk \approx [HCO_3^-] + 2[CO_3^{2-}] \tag{3.6}$$

but only once to DIC (see Equation 2.4). The term $r_{n:p} \cdot PO_4$ corrects the Alk for the addition of protons during the remineralization of organic matter.

Now, C* is a tracer with conservative properties and has no biological sources or sinks in the ocean. Variations in C* are a result of air-sea gas exchange only (Gruber et al., 1999). Therefore, we can use C* together with the TSS-assuption and adjust all C* data to either one of the reference years.

3.2.2 Overcoming the problem of poor data coverage

One big challenge with the eMLR(C*) method is to have enough data from a region for at least two reference years in order to be able to construct statistically significant regression equations. There have been two global survey programs that have produced large carbon data sets; the WOCE/JGOFS (1990 - 1998) (W.R.Wallace, 2001; Key et al., 2004) and the CLIVAR/GO-SHIP program (2000 - precent) (Talley et al., 2016). Although these programs are extensive, the data sets have gaps in both time and space. The lack of data coverage is especially problematic in the Arctic Ocean and Nordic seas, where there are very few cruises from 1994 and 2007.

Further, for the eMLR it is necessary that the two time-separated data sets are from the same place. As an example, Ulfsbo et al. (2018) used repeated sections from 1996 to 2015 in order to estimate anthropogenic uptake for a few specific cross sections in the Arctic Ocean. With the improved method of Clement and Gruber (2018), we can use all the data available in the Arctic Ocean and Nordic seas, instead of being limited to the few repeated sections, as was the case earlier.

Firstly, climatological distributions can be used as input variables in equation 3.4. With climatologies as input, the eMLR(C*) equations can define entire water masses and produce estimates of ΔC_{ant} in 3D, as long as the change in each variable from t_1 to t_2 is small compared to their climatological value.

Secondly, the TSS assumption enables the normalisation of data to a single year, i.e. all data from two eras (here 1991 to 2000, and 2001 to 2015) can be collapsed to a single reference year (here 1994 and 2007). This means that any data collected in the two eras can be used to define the eMLR(C*) equation for one of the reference years. The TSS concept states that if a tracer had an exponential growth rate over a period significantly longer than the "adjustment time" of the tracer, the tracer has reached a transient steady state (Tanhua et al., 2007). The adjustment time is the time it takes for the contribution of tracer's initial conditions to become negligible in the water column. When this happens, the shape of the tracer profile in the water column no longer changes. Since anthropogenic carbon meet the criteria, we can apply the transient steady state on C*, assuming there are constant mixing and circulation in the ocean over time. This means that the change in C* between two years, t_x and t_y, anywhere in the water column are linearly related to the amount of C* at time t_x, with a proportionality factor determined by the relative change in atmospheric CO_2 between t_x and t_y. The TSS framework therefore allows us to adjust all C* data to a given reference year, as done by Clement and Gruber (2018):

$$C^*(t^{ref}) = C^*(t) - \beta(t) \cdot C_{ant}(t^{ref}), \tag{3.7}$$

where $\beta(t) = pCO_2^{atm}(t) - pCO_2^{atm}(t)^{ref} / pCO_2^{atm}(t)^{ref} - pCO_2^{atm}(t)^{pi}$, is the factor given by the change in atmospheric CO_2. $(t)^{ref}$ is the reference year, $(t)^{pi}$ is the preindustrial time with a ppm of 280, and t is the year the data sample was taken (Tanhua et al., 2007; Clement and Gruber, 2018). $C_{ant}(t^{ref})$ is the total C_{ant} content in the water mass for the reference years. These values have to be taken from previous estimates, but there are no estimates of C_{ant} from 1994 and 2007 in the Nordic seas and Arctic Ocean. Therefore, these were generated by adjusting the existing estimates for 2002 (Nordic seas) and 2005 (Arctic Ocean) (Olsen et al., 2010; Tanhua et al., 2009). This adjustment is also carried out using the TSS framework, such that::

$$C_{ant}(t_2) = C_{ant}(t_1) + \alpha \cdot C_{ant}(t_1), \tag{3.8}$$

where t_2 is either one of the reference years (1994 or 2007) and t_1 is 2002 (Nordic Seas, gridded C_{ant} estimates from Olsen et al. (2010)) or 2005 (Arctic Ocean, gridded C_{ant} estimates from Tanhua et al. (2009)).

α was calculated from the change in atmospheric CO_2, the buffer factor, and the disequilibrium factor. Gruber et al. (2018) calculated α to be ~0.26 for the high latitudes between 1994 and 2007. Since I scaled from 2002 and 2005, and not from 1994 to 2007, I calculated new α values. The term with atmospheric CO_2 has the biggest effect on α, and the disequilibrium and buffer factor terms are difficult to calculate for the study area. Therefore, I only adjusted the term with atmospheric CO_2. I ended up with four new values for α: 0.034 and -0.18 to scale C_{ant} from 2005 to 2007 and 1994, and 0.096 and -0.133 for 2002. I also tried other values between -1 and 1 to check the sensitivity of α, but there were actually no visible changes in the plotted ΔC_{ant} results.

When C* is adjusted to the reference years, all the data from the Arctic Ocean and Nordic seas can be used, and not just the data from 1994 and 2007. The data from 1991 to 2000 was normalized to 1994, and the data from 2001 to 2015 was normalized to 2007. Ideally, the reference year should lie in the middle of the intervals, but I chose this division based on the spatial cruise distribution. This division offered the best geographical coverage of cruise data for both reference years. Now, eMLR(C*) equations for each reference year can be computed and used together with the predictor variable climatologies to estimate the change in C$_{ant}$, ΔC_{ant}^{eMLR}, for the entire Nordic Seas and Arctic Ocean.

Reference year 1:

$$C^*(t_1^{ref}) = a_1 + b_1 \cdot V_1(t_1) + c_1 \cdot V_2(t_1) + ... + z_1 \cdot V_k(t_1) + Residuals(t_1), \tag{3.9}$$

Reference year 2:

$$C^*(t_2^{ref}) = a_2 + b_2 \cdot V_1(t_2) + c_2 \cdot V_2(t_2) + ... + z_2 \cdot V_k(t_2) + Residuals(t_2), \tag{3.10}$$

Combined:

$$\Delta C_{ant}^{eMLR(C*)}(t_2^{ref} - t_1^{ref}) = (a_2 - a_1) + (b_2 - b_1) \cdot V_1^{clim} + (c_2 - c_1) \cdot V_2^{clim} + ... + (z_2 - z_1) \cdot V_k^{clim} + (R(t_2) - R(t_1)) \tag{3.11}$$

3.2.3 Selecting predictor variables

It is not possible to define a universal MLR because of differences in preformed values of both DIC and the various potential predictors. There are also different importance of various processes and possibly regional and seasonal variations in the Redfield ratios. Hence, no global MLR equation can be defined and the MLRs are usually determined for specific regions (Carter et al. (2017)), water masses (Ulfsbo et al. (2018)) or depth/density layers (Gruber et al. (2018)). This applies in terms of which predictor variables to use, and in terms of the actual statistical coefficients.
For the best possible fit, the predictor variables should be independent of each other and the relationship between response and predictor variable linear. Friis et al. (2005) used potential temperature, salinity, and silicate as predictor variables, and let the forth variable vary between phosphate, AOU, and nitrate. I will do as Clement and Gruber (2018) and use a purely statistical routine to find the best predictor variables. DIC adjusted for biological processes, C*, is used as the response variable, and nitrate, phosphate, silicate, alkalinity, AOU, temperature, and salinity as *possible* predictor variables. Then, all combinations of variables are tested and the final equations selected based on the statistical robustness of the fit, as expressed by the "root-mean-square-error" (RMSE) of the various regressions.

In this thesis, the Nordic seas and Arctic Ocean were divided into water masses (see Section 3.6). In each water mass, 112 MLRs were generated by using every possible combination with a minimum of 2, and a maximum of 5 predictor variables. I used the MATLAB function *robustfit* to generate the MLRs. From the 112 different MLR-equations, I selected the ten best based on the average RMSE values for t$_1$ and t$_2$. Accordingly, there are now ten equations for t$_1$ and ten equations for t$_2$, equivalent to equation 3.9 and 3.10. The coefficients of each pair were subtracted from each other to create ten estimator equations, such as equation 3.11. Then, the mean result of all ten eMLR(C*) equations were used as the final estimate of ΔC$_{ant}$, see Figure 3.1.

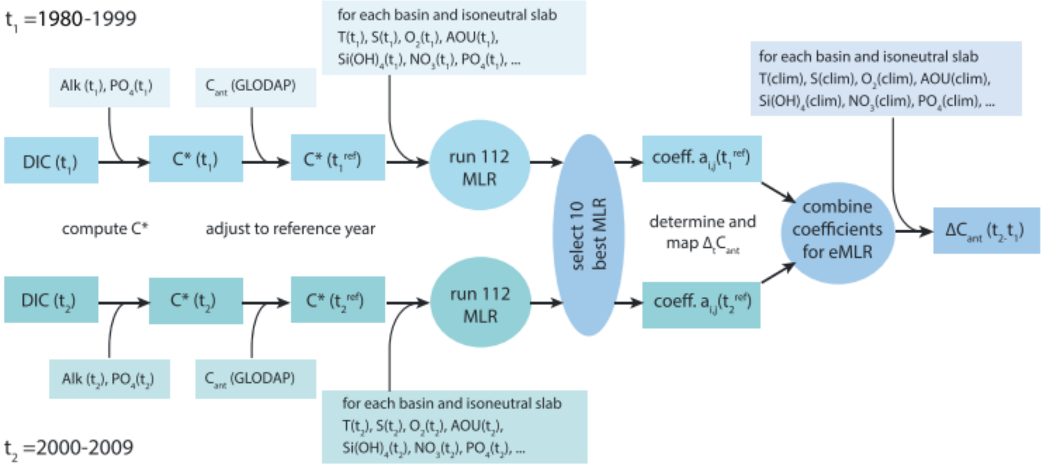

Figure 3.1: The work flow of estimating ΔC_{ant} with the eMLR(C*) method, from Clement and Gruber (2018).

3.2.4 Division between water masses and regions

In order to create robust eMLR(C*) equations, water masses with different properties have to be separated from each other. I used the water mass definitions of Rudels et al. (2012) for the Nordic seas and Arctic Ocean, and created individual eMLR(C*) equations for nine different water masses (see Table 3.1). The upper 100 meters and shelf regions are excluded in order to avoid unduly influence of processes such as river run off, sea ice melt, brine rejection, and seasonal changes. Figure 3.2 shows which regions are included.

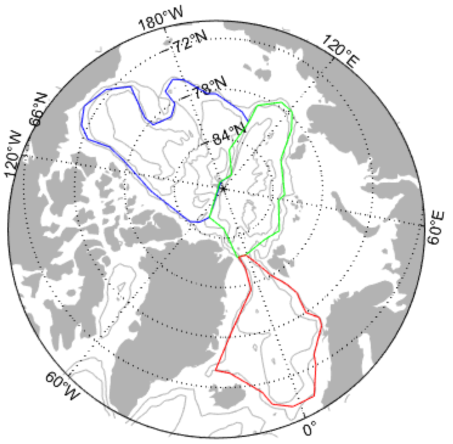

Figure 3.2: Borders around the Canadian Basin, Eurasian Basin, and Nordic seas used to separate the shelf data from the basins. The borders between the Arctic Ocean (including EB and CB) and the Nordic seas were to separate the regions from each other in the eMLR(C*) equations. EB and CB are separated to define uPDW EB and uPDW CB independently.

Water mass	Comments	Area restrictions
PW1	As in Rudels et al., 2012	AO
PW2	———	AO
AAW	———	AO
DAAW	———	AO
uPDW EB	———	EB
uPDW CB	———	CB
AW	removed lower density restriction	none
DAW	lower density restriction modified	NS
AIW	removed lower density restriction	NS

Table 3.1: The nine different water masses used in this thesis. Some of them had to be modified to include all regions in the climatologies. The modifications and area restrictions are listed under comments. The Atlantic Water is restricted to the Nordic seas when I made the eMLR(C*) equations, but it has no area restrictions in the climatologies. AO = Arctic Ocean, NS = Nordic seas.

Clement and Gruber (2018) divided the water masses into isopycnal slabs, and created individual equations for each slab. The assumption is that every slab has similar properties since mixing and ventilation generally happen along isopycnals in the ocean. The density gradients in the Nordic seas and Arctic Ocean are very small, and the density classes used by Clement and Gruber (2018) would therefore include many different water masses if they were used in this region. Ulfsbo et al. (2018) tested the option of using isopycnal slabs, but got unrealistically high ΔC_{ant} values in the deep waters. The deep water of the Eurasian and Canadian basin are between 250 and 450 years old, and it is therefore unlikely that they have high levels of C_{ant}.

I used the water mass definitions of (Rudels et al., 2012) instead of isopycnal slabs since they also include potential temperature, Θ, and salt restrictions. The potential temperature and salt restrictions separate water masses with the same density from each other (see Figure 3.3).

In addition, I used the water mass definitions on the GeoCap climatologies, but some of the definitions had to be modified in order to include all regions in the climatologies. Large areas in the Nordic seas are left blank, especially in the upper 300 meters. Here, the climatologies have places where the density is lighter than 1027.97 at the same time as temperature is below zero. This does not match with either AW or DAW as defined by Rudels et al. (2012). I chose to modify the definitions of AW and DAW to include all empty regions. I also removed the lower density restriction on AIW to include blank regions of water with potential temperature below 0 and potential density below 27.97.
There were three water masses from (Rudels et al., 2012) I could not identify in neither the data or in the climatologies: Canadian Basin Deep Water (CBDW), Eurasian Basin Deep Water (EBDW), and Nordic sea Deep Water (NDW). When I got the first results, the uPDW covered the entire Arctic Ocean below 1000 meters. The C_{ant} below 2000 meters in both basins were suspiciously high, reaching 12 μmol/kg at some places. According to Tanhua et al. (2009) and Ulfsbo et al. (2018), there should not be any C_{ant} at these depths. Since CBDW and EBDW have different properties, I

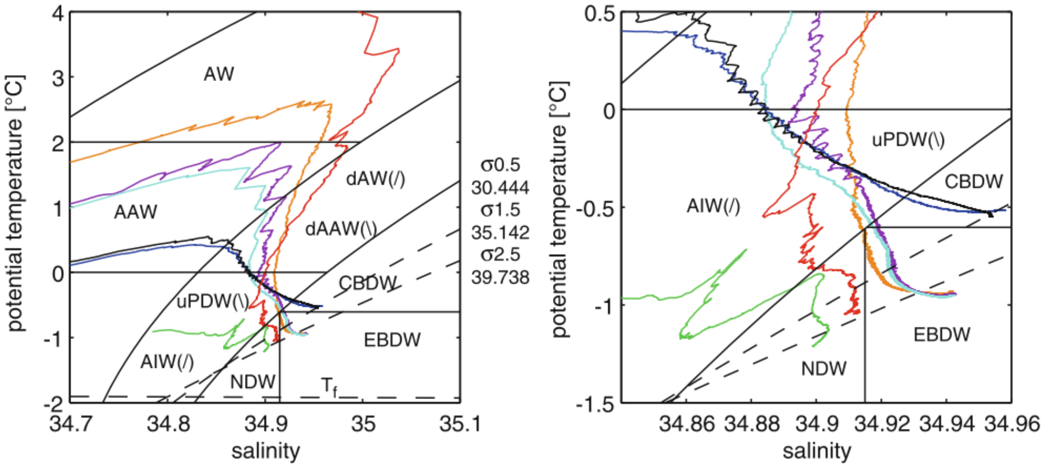

Figure 3.3: ΘS plots from a) the Arctic Ocean and Nordic seas water masses, b) the Arctic Ocean water masses. The Red line represents the Fram Strait (West Spitsbergen Current); orange - Nansen Basin (Fram Strait branch), purple - Nansen Basin interior, light blue - Amundsen Basin, black - Makarov Basin, blue - Canadian Basin, and green - the Greenland Sea (Rudels et al., 2012).

divided uPDW into two parts; uPDW CB for the Canadian Basin and uPDW EB for the Eurasian Basin. Ideally, the deep water should be separated from uPDW, but there is no apparent way of doing this. I tried separating at different depths between 1500 and 2500 meters, since this is where the literature states that the deep water begins (Bluhm et al., 2015, Rudels et al., 2012), but they all resulted in high increase of C_{ant} at the bottom. By dividing only into uPDW CB and uPDW EB, I got rid of the high uptake in the deepest parts of CB, but the C_{ant} increase estimated for the deepest part of the EB still seems unrealistically high (see Section 4.3). For future studies there should be a way to identify CBDW and EBDW since that would potentially lead to more precise results. I did not compensate for the lack of NDW since the uptake looks reasonable at all depths in the Nordic seas (see Chapter 4).

3.3 Making climatologies with GeoCap

GeoCap is a software originally used to model geological structures. It has many similarities with Matlab since it can run scripts and do mathematical calculations. In addition, it is built on top of a 3D system, and is therefore a great visualization tool. To create the climatologies, I used a plug-in to GeoCap developed by ModelGeo AS, originally meant for petroleum geology. ModelGeo helped me adjust it for oceanographic use.
See https://www.geocap.no/products-and-services/geocap-desktop?originId=3689
and https://geocap.atlassian.net/wiki/spaces/ug/pages/7372985/Geocap+Main

Originally, I planned to use the climatologies from GLODAP version 2 (Lauvset et al., 2016) and World Ocean Atlas (WOA) (*https://www.nodc.noaa.gov/OC5/woa18/woa18data.html*). Unfortunately, the GLODAP climatologies contains many blanked out grid cells because of unacceptable uncertainty of the mapped values. This is especially a problem in the Eurasian and Canadian Basin.

WOA contains blanked out grid cells for temperature and salinity, and do not have grids below 500 meters. In my studies, I needed mapped climatologies for all depths since I wanted to calculate the column inventories of ΔC_{ant}. Since more data have become available after the GLODAP and WOA climatologies were made, I can make new climatologies for all the variables I need in this thesis.

I used GeoCap to create climatologies of every variable needed as input in the eMLR(C*) equations. These variables are temperature, salinity, alkalinity, AOU, nitrate, phosphate, and silicate. In addition, I prepared climatologies of potential temperature and density. These climatologies are needed to identify the regions and depths where to apply the various eMLR(C*) equations, as these were developed on a water mass basis, as described above.

3.3.1 Gridding routine

GeoCap makes regular 3D-cubes with fixed distances in the x, y, and z direction of observed irregular input data, and lets you choose between different types of gridding and smoothing. For the climatologies in this theses, a single grid cell is 20.000 * 20.000 meters. In the vertical, I created a layer for every 10 meters. The observations are first linearly interpolated to every layer in the vertical direction. The closest observation above and below a layer is used for the interpolation. Then, all the grids are modelled independently. I used what is called ”parabolic interpolation” for every grid, and medium to low smoothing. GeoCap grids horizontally on each layer and extrapolates to the borders. I chose to not let it extrapolate vertically. After each layer is modelled, the cube is cut against topography.

Next, the surfaces were interpolated to 33 standard depths similar to GLODAPv2 and WOA and exported to MATLAB. Since my goal is to determine the increase in column inventory of anthropogenic CO_2, it is important that the interpolated layers represent a typical value. Therefore, I used the vertical mean values of every interval when I made the 33 layers. Each interval lies symmetrically around each layer.

There is very little alkalinity data for the Arctic Ocean and Nordic seas, which resulted in an unrealistic looking alkalinity climatology at first try. Each grid had circular features - ”bulls eyes”, around the location of the original observations since GeoCap could not identify a clear pattern in the data. Alkalinity is important for the ΔC_{ant} results since it is included in most of the eMLR(C*) equations, as seen from Table 4.1. Therefore, in order to make a better alkalinity climatology, I correlated the observed alkalinity data with the collocated values extracted from the salinity climatology and used the relationship to make a new alkalinity climatology based on the existing salinity climatology. The linear regressions were made for three different water masses:

1) Atlantic Water; $T > 0$, $S > 34.92$, after Walczowski (2013).
2) Deep water: $S > 32$ & $S < 34.92$.
3) Surface water: $S < 32$.

All data above 100 meters were excluded from the regression. The Atlantic Water definition includes Atlantic origin water in both the Arctic Ocean and Nordic seas. The R^2 statistics of the three correlations are 0.54, 0.45, and 0.57 for the three water masses.

Specifically, the mapped climatologies for salinity and temperature were used to define the distribution of the three water masses. Then, each regression equation was used on the different water masses in the salinity climatology, to generate the alkalinity climatology. To make the mapped alkalinity climatology more accurate, the residuals from the regression analysis were used to adjust it. This is done by making a new climatology from the residuals and simply add it to the alkalinity. Generally, there are two ways of making the residual cube; 1) let each residual influence a distance around it defined by a fixed radius, or 2) let GeoCap find isolines through in the residual data and map each surface in the climatology based on this. To decide which gridding method to use, the residuals were analysed in a variogram. A variogram describes the spacial interdependency of the data. If the difference in residuals are constant after they reach a certain distance, they are said to be *stationary.* If the difference between the residuals increases the further away they are from each other, they are *non-stationary.* In this case, the residuals are non-stationary, and therefore the best choice was to map them with method number 2.

Chapter 4

Results

4.1 GeoCap climatologies

Figure 4.1 to 4.7 show the GeoCap climatologies for all variables at 125 meters. We can clearly see how the warm, saline, Atlantic Water flows northward through the Nordic seas and into the Arctic Ocean. The nutrient rich upper halocline in the Canadian Basin (Rudels et al., 2012), is also clearly present, with very high values of silicate, phosphate and AOU, for instance.

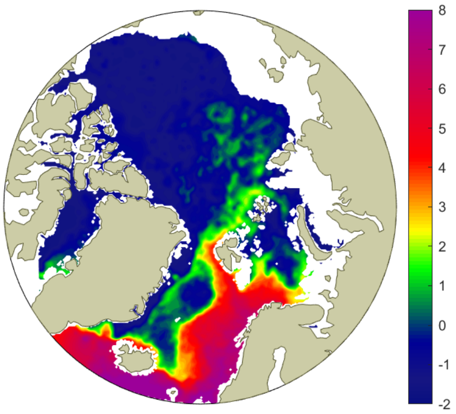

Figure 4.1: Temperature at 125 meters.

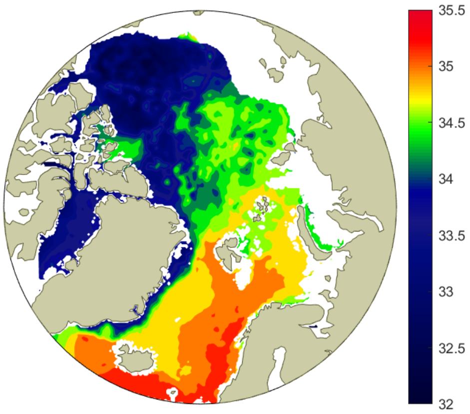

Figure 4.2: Salinity at 125 meters.

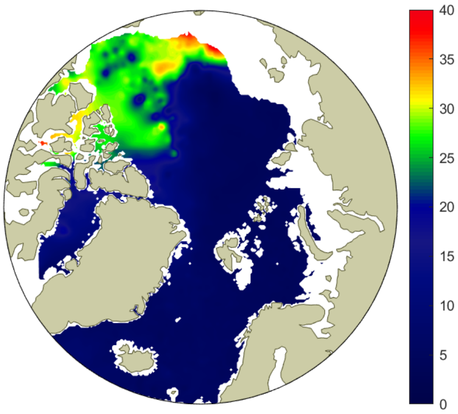

Figure 4.3: Silicate at 125 meters.

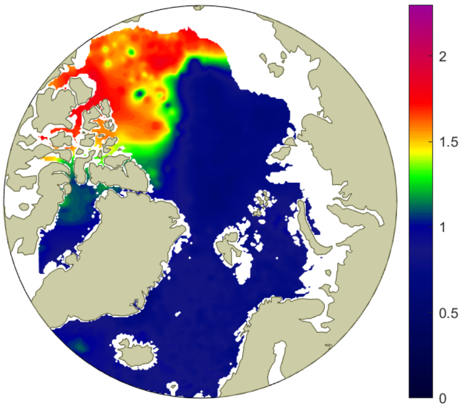

Figure 4.4: Phosphate at 125 meters.

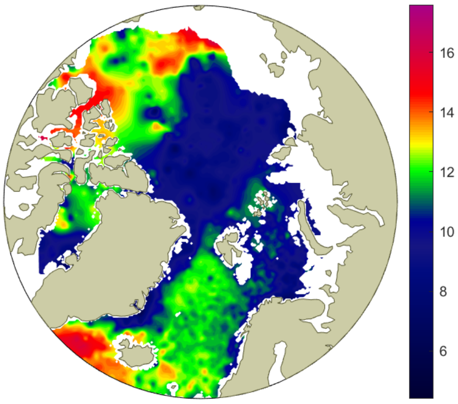

Figure 4.5: Nitrate at 125 meters.

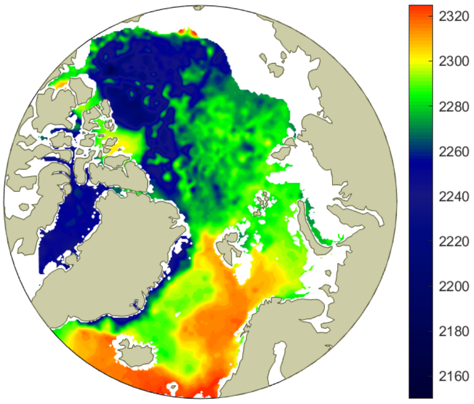

Figure 4.6: Alkalinity at 125 meters.

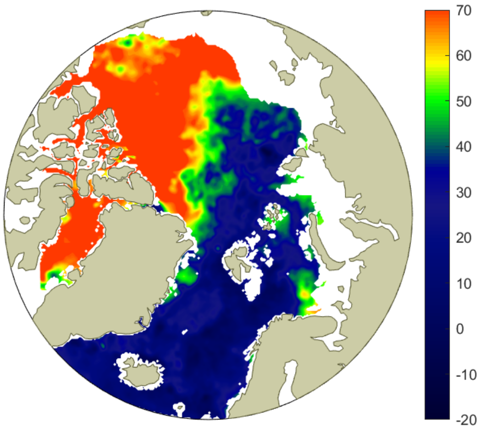

Figure 4.7: AOU at 125 meters.

4.2 eMLR(C*) equations and predicted C*

Water mass	Number of times variables were used in the 10 best equations						
	S	T	AOU	TAlk	NO_3^-	PO_4^{3-}	SiO_2
PW1	6	7	8	6	4	10	7
PW2	2	6	8	7	7	6	10
AAW	4	5	4	10	8	10	6
DAAW	3	10	4	10	4	10	3
uPDW EB	7	4	7	10	1	10	4
uPDW CB	9	4	10	8	4	4	7
AW	5	10	6	8	4	10	3
DAW	6	10	4	10	4	8	5
AIW	2	4	7	10	4	10	6
Total	44	60	58	79	40	78	51

Table 4.1: The number of times each variable appear in the ten best eMLR(C*) equations for each water mass.

Table 4.1 shows that alkalinity and phosphate are variables that are most frequently used in the eMLR(C*) equations, while salinity and nitrate are the least selected. Alkalinity affects the solubility of C_{ant} through its impact on the buffer capacity, and is as such expected to be important for the equations. Alkalinity and salinity are usually well correlated, but in the Arctic Ocean, Russian river input carrying alkalinity might decouple this relationship. Therefore, salinity is not chosen as many times as alkalinity. Nitrate can be affected by denitrification, and this non-conservative behaviour likely explains why phosphate and not nitrate is, broadly, the preferred nutrient variable in the equations.

Figure 4.8 illustrate the RMSEs of the ten best equations for each water mass. The RMSEs represent the spread of residuals around the best fitted regression line. A low value represents a better fitted regression line than a high value. The RMSEs in Table 4.8 range from 3 in AW to 7.1 in PW1, and are quite similar to the RMSEs of Clement and Gruber (2018) for the Atlantic Ocean. In general, the Nordic seas' water masses have lower RMSEs than the water masses of the Arctic Ocean, indicating that the equations fit better for the Nordic seas. PW1 and PW2 are especially high because they are the upper waters and actually consist of several different water types, including shelf water affected by local processes.

Figure 4.9 shows that for all of the water masses, except uPDW CB, C* has increased from 1994 to 2007, and as such likely reflects the increase in C_{ant}. PW2 and DAW seem to have the highest increase of about 20 μmol/kg, but there is little data from the 1994 period. PW1 and AW also have little data from 1994 compared to 2007.

By comparing the predicted C*, $C*_{pred}$ with the "observed" C*, $C*_{obs}$, we can check how well the water mass definitions fit with its respective data set. If the fit between $C*_{pred}$ and $C*_{obs}$ show a linear relationship without any features of particularly biased data off the overall line, the eMLR(C*) equations are successfully describing the entire water mass as there is consistency in the

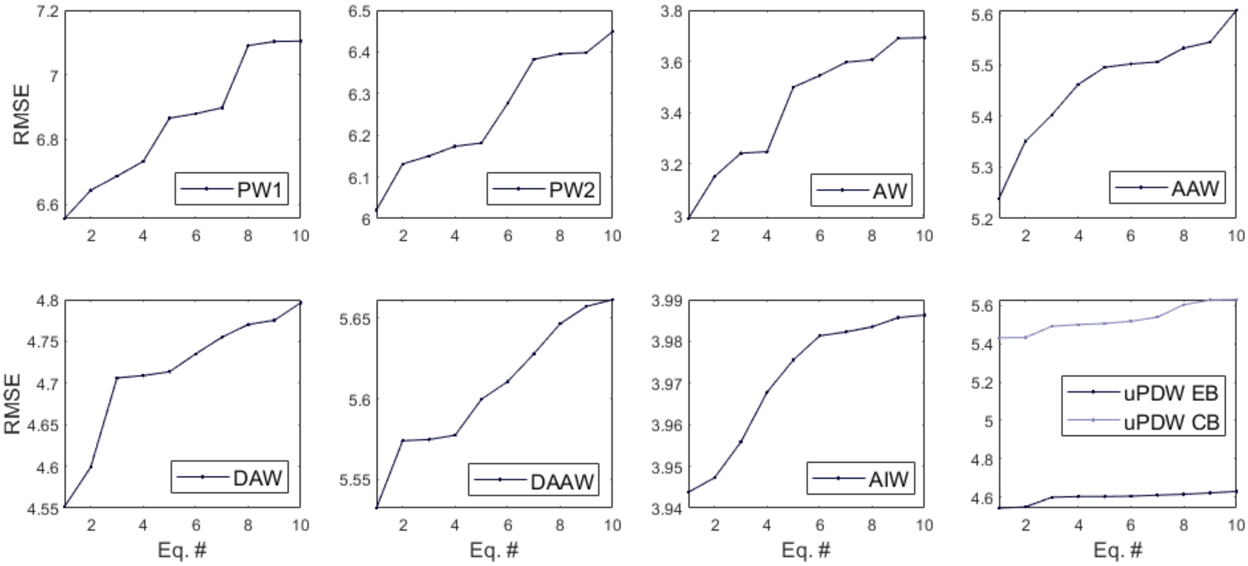

Figure 4.8: RMSE values of the 10 best equations for each water mass. Lower RMSE values represent less uncertainty and better fits for the regression analysis.

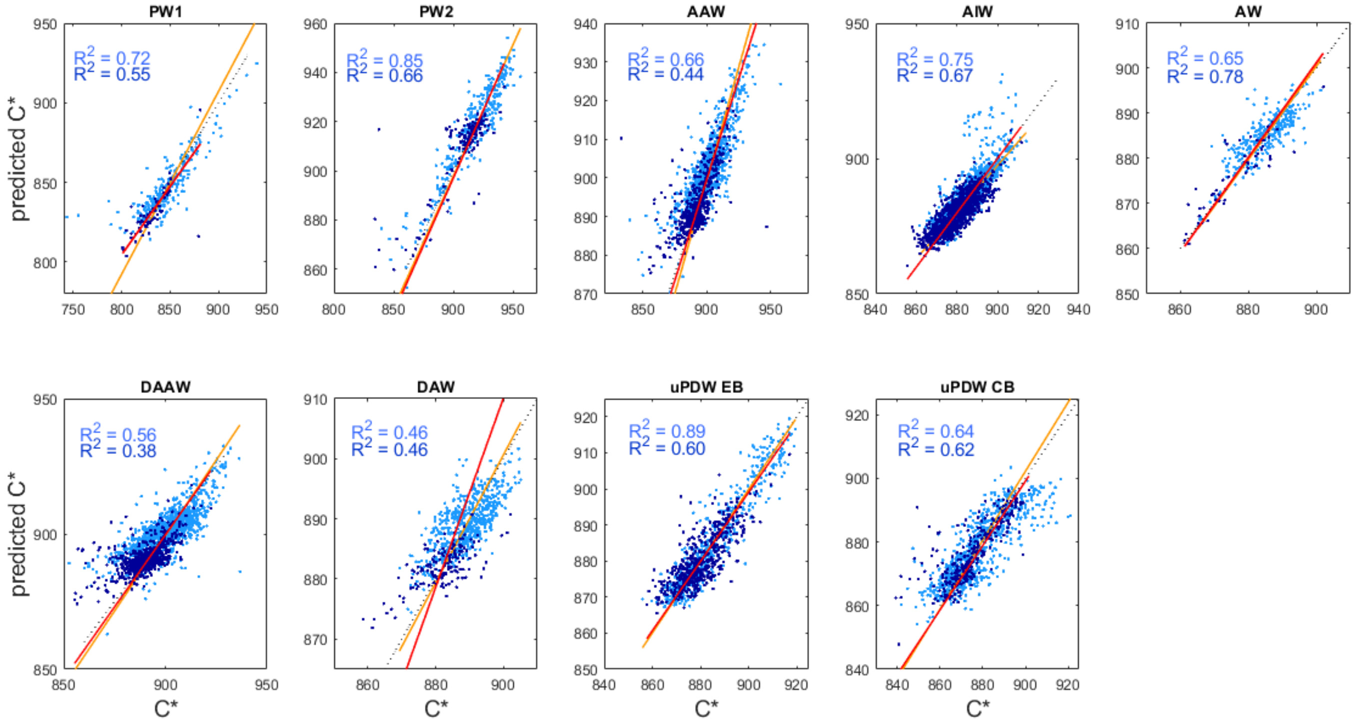

Figure 4.9: The mean of the 10 predicted C* values plotted against "observed" C* for each reference year. The dark blue dots are the data from the 1994 period and the light blue dots the 2007 period. The R^2 values are also shown in each subplot. The gray, dotted, line behind the data is the 1:1 relationship, representing a perfect fit between predicted C* and "observed" C*. The red line is the regression line for the 1994 data, and the orange for 2007.

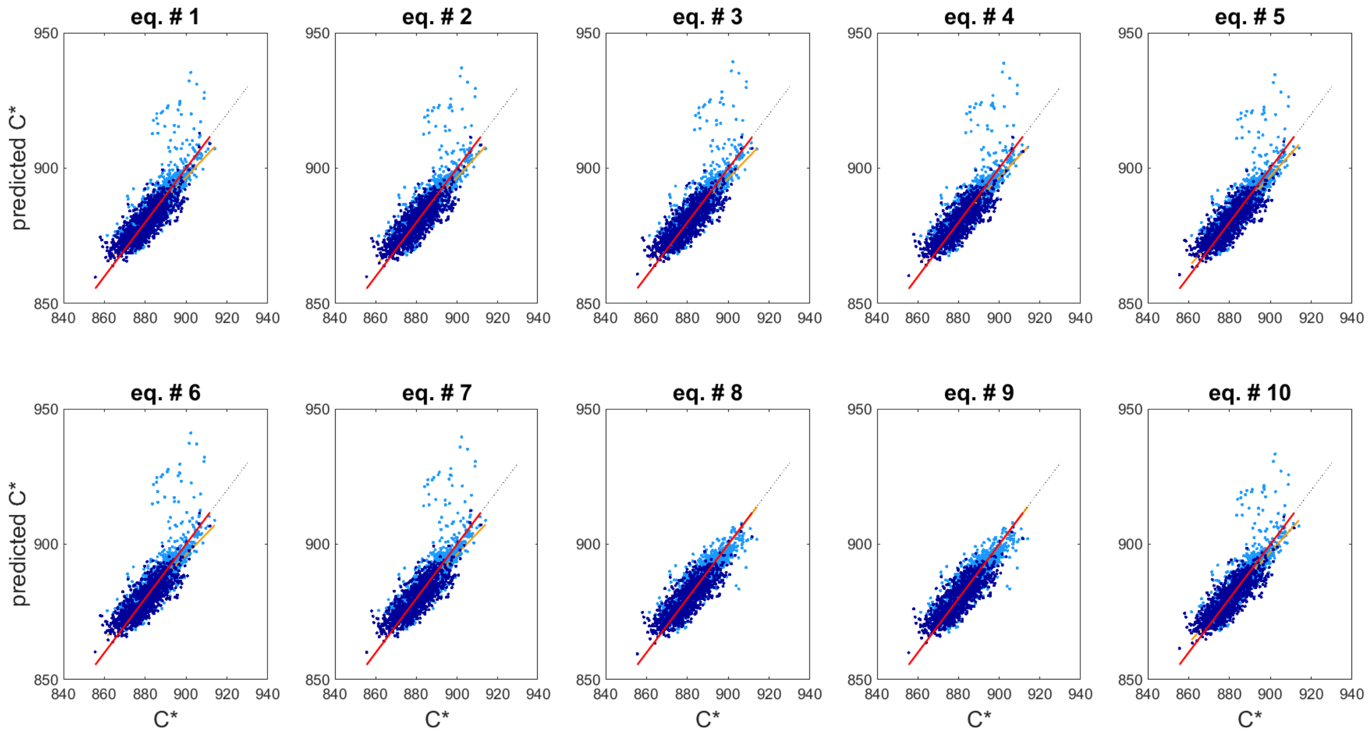

Figure 4.10: The mean of the 10 predicted C* values plotted against "observed" C* for each reference year for AIW. Equation number 8 and 9 do not have the large scatter above the regression line as the other equations, indicating that these equations describe the water mass better than the others.

relationship throughout the water mass. On the other hand, if there is a large scatter on either side of the line, it means that the eMLR(C*) equations are not able to describe all parts of the water mass, which may give rise to errors in the results.

From Figure 4.9, it looks like most of the water masses are well defined with only a few data points off the linear relationship. Also PW1 and PW2 have relatively little scatter, despite the relatively high RMSE values, mentioned above. However, PW2 has some points with high C^*_{pred} values compared to C^*_{obs} at the lower end of the scale. The same is true for AAW and DAAW. uPDW EB has little scatter, and the same is the case for AW and DAW. uPDW CB is more spread on both sides of the linear fit compared to the other water masses. This is expected as we know there are two water masses included in uPDW CB (Section 3.2.4). This is also the case for uPDW EB. Regardless, the eMLR(C*) equations clearly reproduce the overall features of C* in these two water masses.

AIW has a few points with high C^*_{pred} values. We know there is missing a water mass in the Nordic seas, namely the Nordic seas Deep Water. The high values might belong to NDW as this was identified as AIW when following Rudels et al. (2012). If a few points from another water mass with different relationship between the variables are included in AIW, it can result in scatter outside the linear relationship, as shown in Figure 4.9. Figure 4.10 show predicted vs. observed C* for each of the ten equations that define AIW. Equation 8 and 9 clearly predict the AIW C* variability the best, caused by inclusion of salinity.

4.3 The increase of anthropogenic CO_2 in the Nordic seas and Arctic Ocean, 1994-2007

4.3.1 Nordic seas

The estimated uptake and C_{ant} column inventories increase between 1994 and 2007 are shown in Figure 4.11, 4.12, and 4.13. Figure 4.11 also shows the water mass distribution. At all depths, of the Nordic seas show an increase of anthropogenic CO_2, except in the most western parts, near the East Greenland Current at 100 m, Figure 4.11. The highest ΔC_{ant} values are found in the Lofoten Basin, with a maximum of about 16 μmol/kg from 100 meters and down to about 800 m. In general, the lowest increase is in the deepest parts of the Nordic seas, around 3 - 4 μmol/kg. There is in general higher increase in the upper eastern part of the Nordic seas where AW and DAW are located. AIW is the dominating water mass from about 800 and down, but is present in the Greenland and Iceland Sea up to 100 m. The increase of C_{ant} in the Iceland Sea is highest at 100 meters and gradually decreases towards the bottom. In the central Greenland Sea, fairly high ΔC_{ant} values, of 7 umol/kg, are found all the way down to 1200 m.

The features described above, broadly aligns with the expected features of C_{ant} increase in the Nordic seas. The water masses are relatively young because of the vertical transportation of modified AW that ventilates the intermediate and deep water masses (Jeansson et al., 2011). Therefore, we expect C_{ant} to increase in the entire Nordic seas. We also predict the largest increase in the Atlantic derived water masses (AW and DAW) since these water masses are saturated with C_{ant} from lower latitudes when they enter the Nordic seas (Anderson and Olsen, 2002). In addition, the buffer capacity is high in these water masses, as they are warm (relatively little natural DIC) and saline (high alkalinity) (see Section 2.2). Therefore, the Atlantic derived water masses have a higher uptake potential for C_{ant} than AIW, which is colder, has lower alkalinity, and is older. Finally, we anticipate higher increase at depth in regions where there is vertical transport of water downward from the surface. This happens in the Greenland Sea, Iceland Sea, and Lofoten Basin, but also where modified re-circulating AW cools and becomes dense. This happens in the north-west part of the Nordic seas (Brakstad et al., 2019, Bosse et al., 2018, Mauritzen, 1996, Eldevik et al., 2009).

My results correspond well with previous studies from these areas. Olsen et al. (2006) estimated the increase of C_{ant} from 1981 to 2002/2003 in the Nordic seas, while Olsen et al. (2010) determined the total uptake since pre-industrial times. Although they study a different period, the patterns are comparable. Especially the pattern in Figure 6 from Olsen et al. (2006) is relevant, since the figure illustrates the estimated increase over a fairly short period, 1981 to 2002/2003, similar to what I do. The most significant differences between Figure 6 in Olsen et al. (2006) and the results presented here occur in the Greenland Sea. Olsen et al.'s Figure 6 shows higher uptake in the upper 1500 meters compared to the present results. At 100 meters, it is ~6 μmol/kg higher than my estimates. The difference between the Lofoten Basin and the Greenland Sea in the upper 100 - 500 meters is also higher in the present results. Here, the estimated increase In the upper 700 meters of the Lofoten Basin is about twice as large as the increase in the Greenland Sea, while according to Olsen et al. (2006) it is only a few μmol/kg higher (their Figure 6). The increase in the Greenland Sea is also more uniform through the water column in my figures.

4.3.2 Arctic Ocean

The highest increase in the Arctic Ocean is found in the PW2 and AAW in the Eurasian Basin and Makarov Basin at 100 meters. Here, the increase reaches 35 - 40 μmol/kg at some places (see 100 meter panel in Figure 4.11). This is the largest increase in both the Arctic Ocean and the Nordic seas. There are also a few places down to 250 meters where PW2 has high increase (see 250 meter panel).

The increase in the Canadian Basin varies a lot at 100 meters. PW1 is the dominating water mass with an average increase of -7.2 μmol/kg, but some places it reaches 10 - 25 μmol/kg. Negative values are not realistic, and the lower limit is therefore set to 0 μmol/kg in the maps. Gruber et al. (2018) chose to replace all negative values with 0. However, to show that the eMLR(C*) method does not work well for all water masses, I kept the negative ΔC_{ant} in the data set, as can be seen in Table 5.1, Table 5.2, and Figure Revelle profile .

From 100 to 700 meters, the mean increase gradually becomes smaller. At 700 meters, the increase is around 8 μmol/kg, with some local variations. The increase is in general lower in the Canadian Basin, especially on the Pacific side, and higher above the Lomonosov ridge. The increase is particularly large north of the Laptev Sea. All water masses from 100 - 700 meters show high ΔC_{ant} values at this place. At 800 meters, there is a large gradient between uPDW EB/uPDW CB and DAAW that appears unrealistic. Here, DAAW has an increase of about 7 μmol/kg, while uPDW EB/uPDW CB have an uptake of 15 μmol/kg. Because of this, there is a unrealistically sharp gradient of ΔC_{ant} between 700 and 800 meters, visible in the 800 meter panel in Figure 4.11. From 800 to 2500 meters, the uptake gradually decreases to 0 μmol/kg in the Canadian Basin and 2 - 4 μmol/kg in the Eurasian Basin. Below this, the uptake does not change much towards the bottom of the sea.

We expect relatively high uptake in AAW and DAAW since these water masses are modified Atlantic water masses. AW enters the Arctic Ocean through the Fram strait and Barents Sea, and is already fully saturated with C_{ant} from lower latitudes (Anderson and Olsen, 2002; Jeansson et al., 2011). In the water mass definitions, AAW and DAAW cover the entire Arctic Ocean from 300 - 700 meters. Ulfsbo et al. (2018) present several cross sections showing ΔC_{ant} across the Eurasian and Makarov Basins. They found an increase of 2.5 - 12.5 μmol/kg from 1996 to 2011 at 300 - 700 meters across the middle of the Eurasian Basin, with most values ranging from 7 - 12 μmol/kg. My results agree quite well with this, although we expect the results of Ulfsbo et al. (2018) to be a bit higher since their time period is two years longer than ours. Below 700 meters, ΔC_{ant} gradually decreases to 0 μmol/kg at about 2000 meters in Ulfsbo et al. (2018). This is different from the results, which have higher values at these depths. In the Eurasian Basin an increase in C_{ant} was detected all the way to the bottom. This is expected, since the Nansen Basin receives dense water from the Barents Sea, as described in Section 2.3. There is no detectable increase in C_{ant} below 2500 meters in the Canadian Basin, which corresponds well with expectations since the water masses here are old (Bluhm et al., 2015). The ΔC_{ant} estimates in the upper 300 meters are higher than Ulfsbo et al. (2018), especially at 100 meters. The differences might arise from the fact that Ulfsbo et al. (2018) define the upper water masses as AAW, not PW1/PW2.

If we assume that circulation and water masses have remained in steady state since pre-industrial times, we can compare the results with Tanhua et al. (2009). They estimated the total uptake of C_{ant} in the Arctic Ocean normalized to 2005. We compared the patterns in their Figure 6 to the ΔC_{ant} estimates in Figure 4.11. Figure 6 shows the distribution of C_{ant} increase at selected depths. The patterns show similarities to my estimates of ΔC_{ant} at ~2000 meters and below. They also show relatively high increase in the area north of Laptev Sea at all depths above ~1500 meters, similar to the increase in this area in my results, as seen from Figure 4.11. Apart from that, the uptake patterns are quite different. Especially when it comes to the sudden gradient between DAAW and uPDW at ~800 meters, that results in higher values of ΔC_{ant} at 1000 meters than 400 meters in my estimates. There is no such gradient in the estimates of Tanhua et al. (2009).

4.3.3 ΔC_{ant} column inventories

Figure 4.12a show the estimated increase in the column inventories of C_{ant} in the Nordic seas. Of course, it is strongly dependent on water column depth, and is highest in the deepest parts. The highest values are found in the Lofoten Basin, followed by the Norwegian and Greenland Sea. The region north of the Greenland Sea also has quite high column inventories. This fits with our expectations since C_{ant} saturated Atlantic water travels through the eastern part of the Nordic seas and gets partially re-circulated west of Svalbard.

The column inventories in the Lofoten Basin are especially high. This is due to the deep convection that takes place down to ~500 meters in this area, plus the permanent "Lofoten Basin Eddie" bringing water further down to ~1200 meters (Bosse et al., 2018). The Greenland Sea is heavily ventilated, and the high inventory in this region is expected. The column inventories in the Iceland Sea are about half those in deep basins. This is largely explained by the shallow depths of the Iceland Sea. Figure 4.12b shows the column inventories of the Nordic seas below 1000 meters. Here, the column inventories in the Greenland Sea are highest, reflecting the deep convection that takes place here.

The column inventories of C_{ant} in the Arctic Ocean is shown in Figure 4.13 and 4.14. They are higher than the Nordic seas, especially in the Eurasian Basin, and there is a sharp gradient between the water masses of the Nordic seas and Arctic Ocean in the Fram Strait. The high column inventories in the Arctic Ocean is related to the high the ΔC_{ant} values in the uPDW EB/CB, PW2 and upper 250 meters of AAW. Figure 1 in Khatiwala et al. (2013) show the column inventories in the Nordic seas and Arctic ocean based on Olsen et al. (2010) and Tanhua et al. (2009). In this figure, the column inventories of C_{ant} are highest in the Nordic seas, which is the opposite of my figures. There is also no gradient in the Fram Strait, reflecting more realistic estimates of the column inventories.

100 m

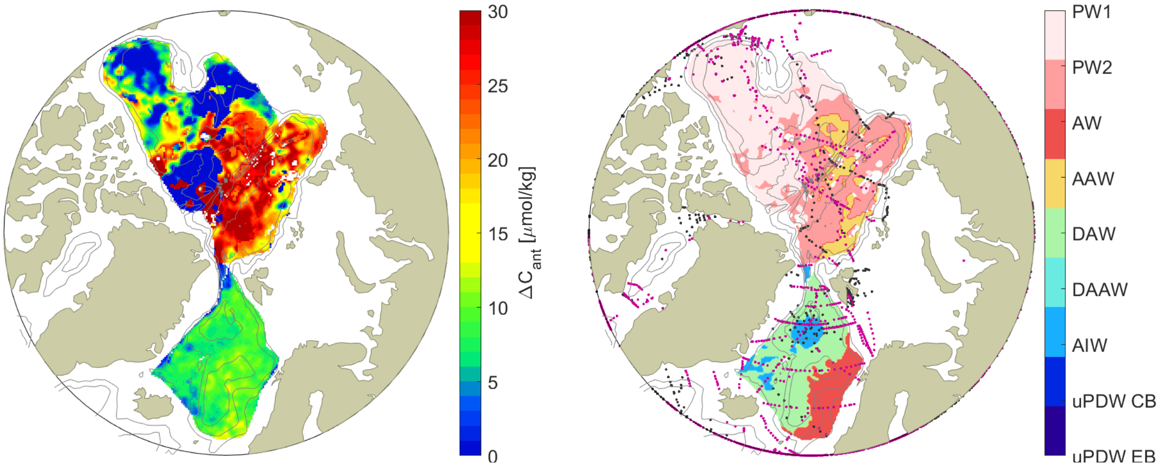

200 m

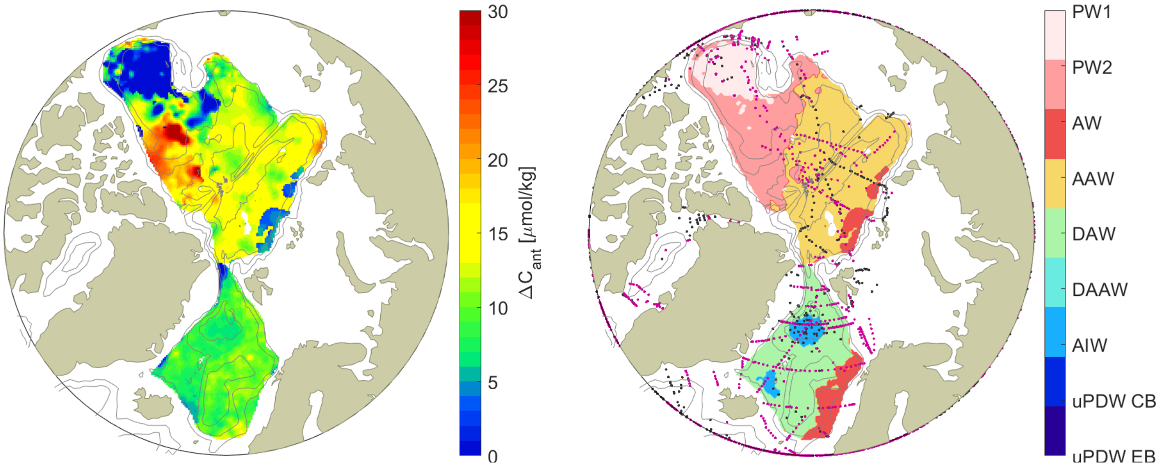

300 m

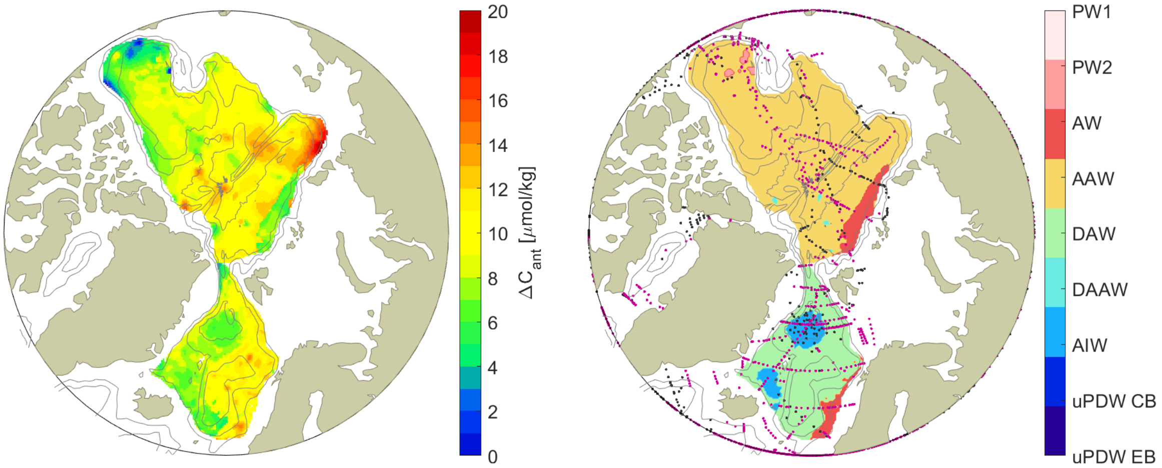

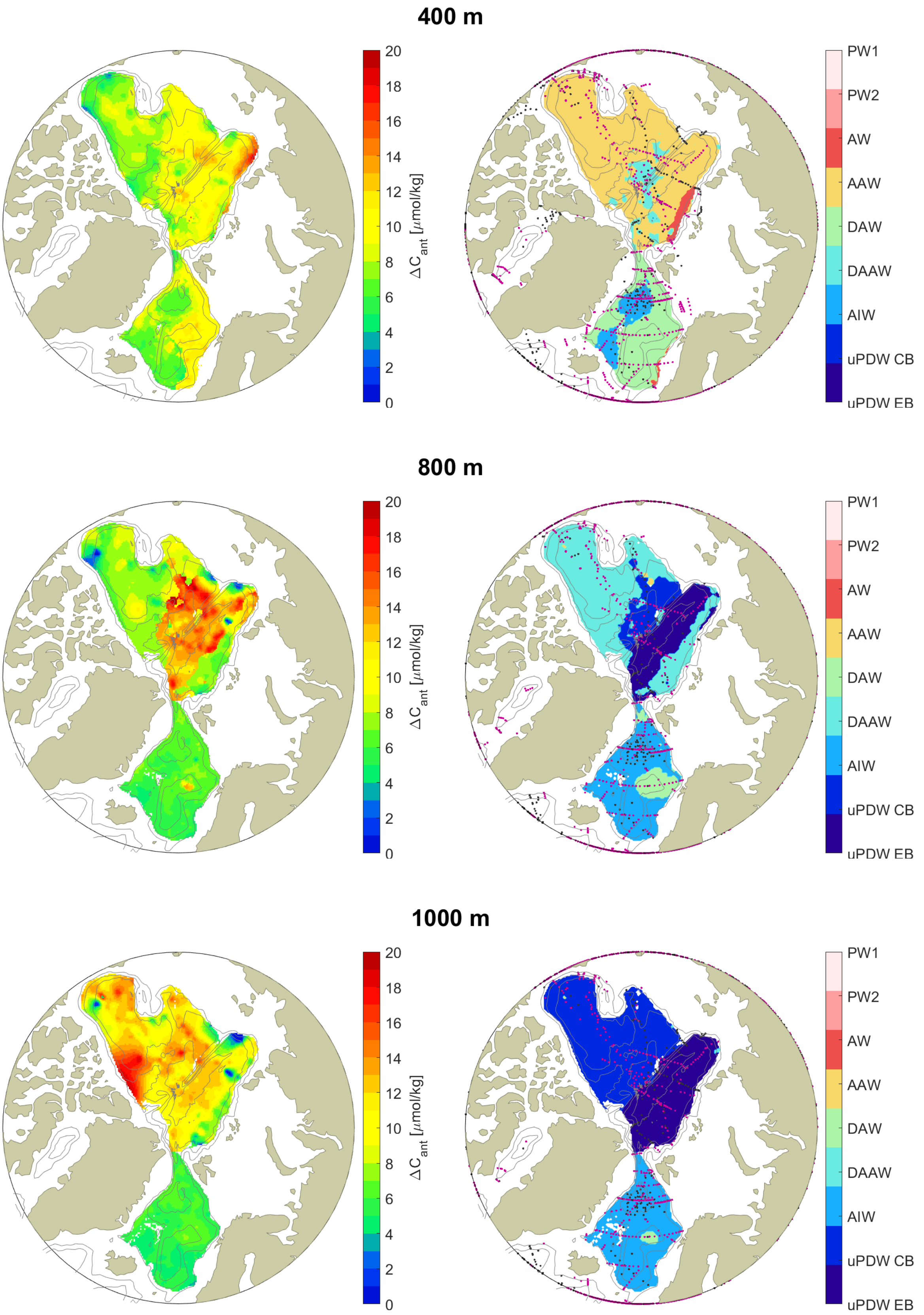
400 m
20
18
16
14
12
10
8
6
4
2
0
ΔC_{ant} [μmol/kg]
PW1
PW2
AW
AAW
DAW
DAAW
AIW
uPDW CB
uPDW EB
800 m
20
18
16
14
12
10
8
6
4
2
0
ΔC_{ant} [μmol/kg]
PW1
PW2
AW
AAW
DAW
DAAW
AIW
uPDW CB
uPDW EB
1000 m
20
18
16
14
12
10
8
6
4
2
0
ΔC_{ant} [μmol/kg]
PW1
PW2
AW
AAW
DAW
DAAW
AIW
uPDW CB
uPDW EB

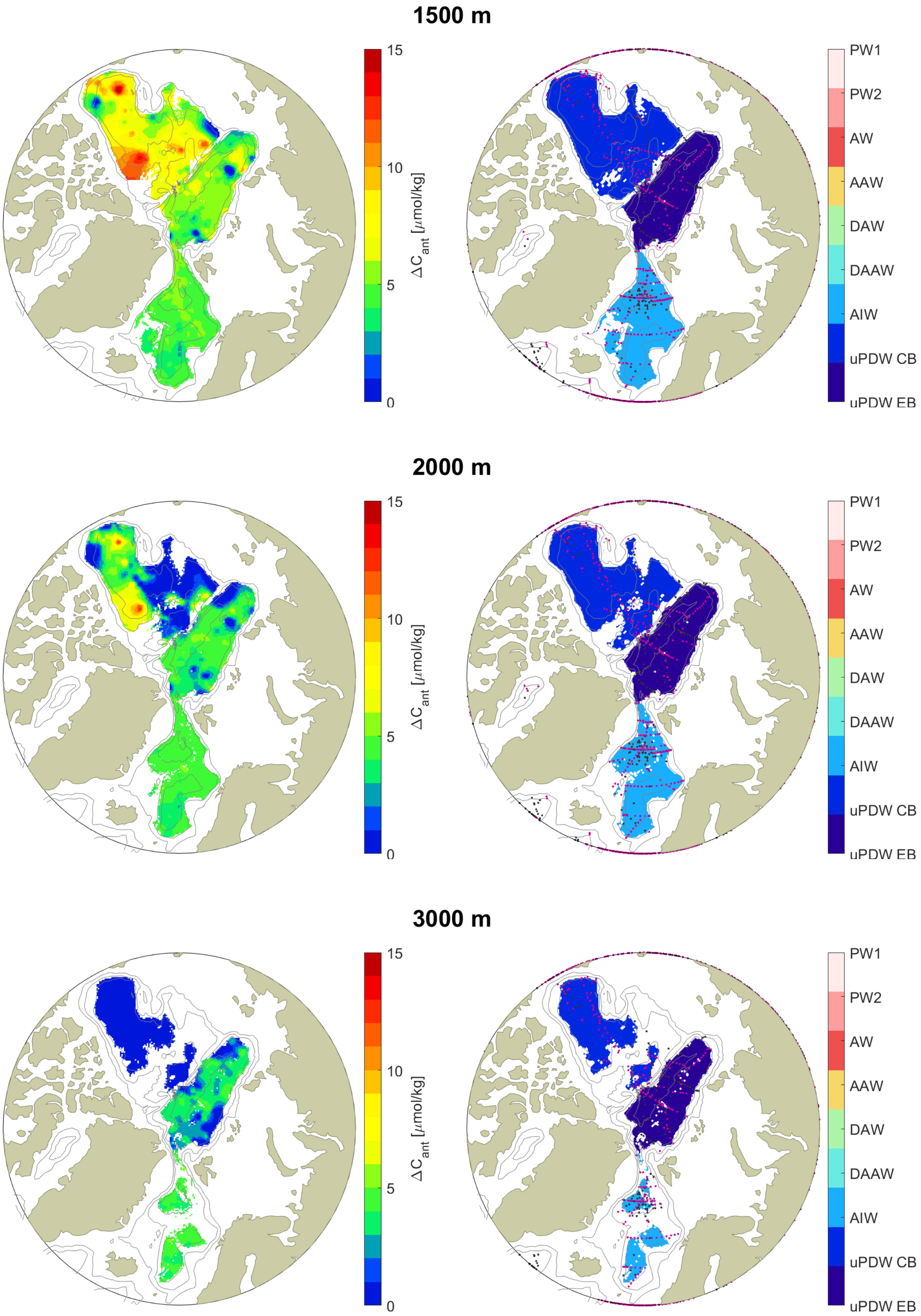

Figure 4.11: ΔC_{ant} to the left and water masses on the right. The black dots on the water mass maps shows data from 1994, and the red dots are from 2007. Note that the colorbar scale are changing.

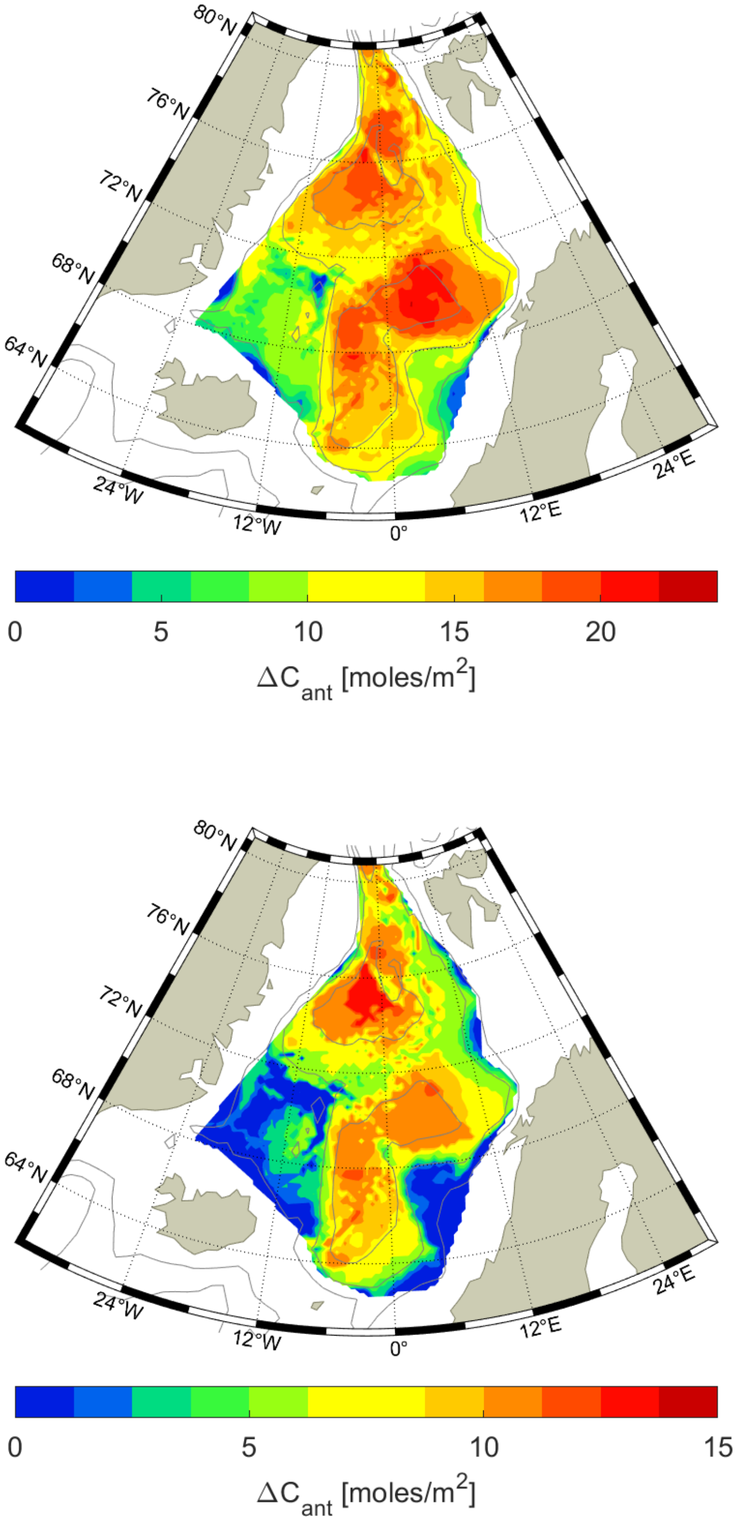

Figure 4.12: ΔC_{ant} inventory in the Nordic seas. a) shows the inventory of the entire water column except for the upper 100 meters. Figure b) shows the inventory of from 1000 meters and down to the bottom. The Lofoten Basin has the highest inventory in the Nordic seas, while the Greenland Sea has the highest inventory below 1000 meters because of the deep ventilation.

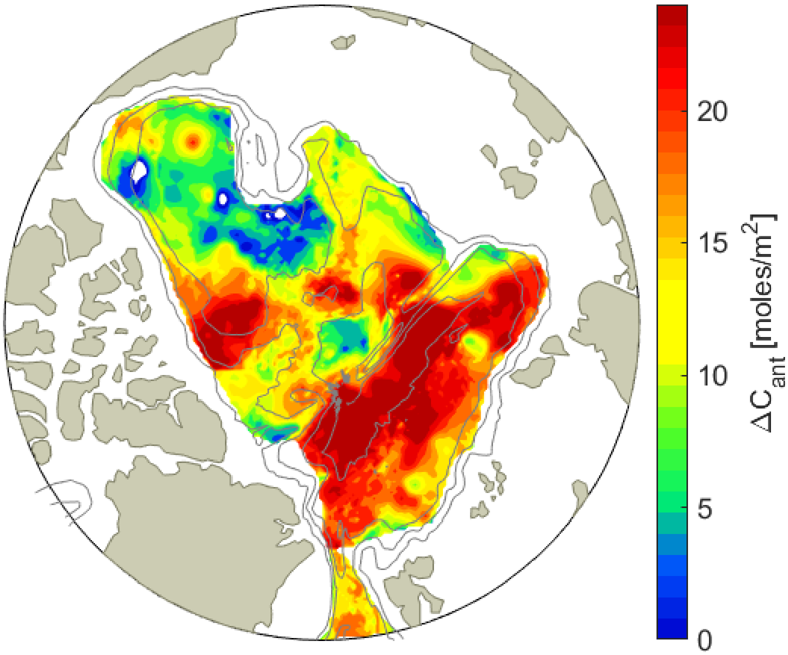

Figure 4.13: ΔC_{ant} inventory in the Arctic Ocean.

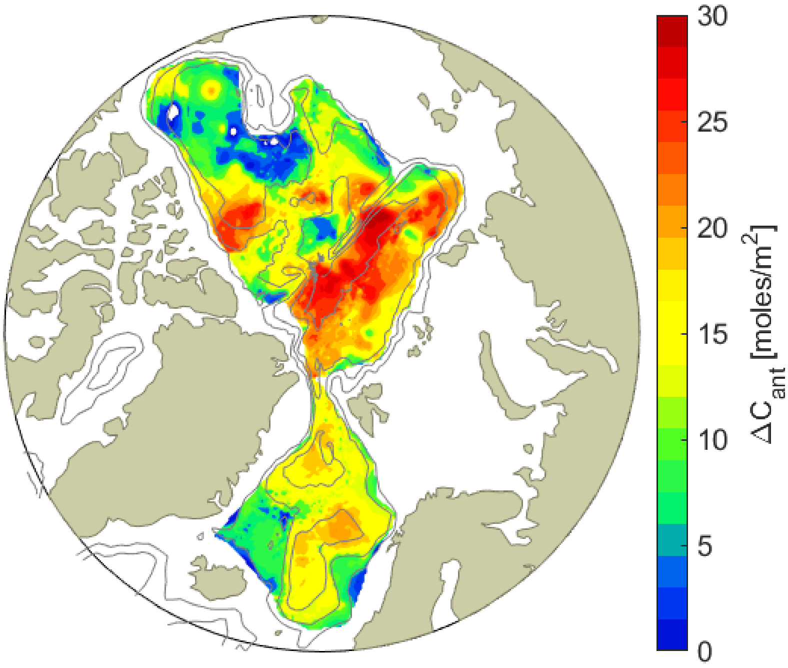

Figure 4.14: Combined inventory of ΔC_{ant} in the Arctic Ocean and Nordic seas.

Chapter 5

Discussion

5.1 Trends in C*

In order to evaluate to which extent the estimated increase in anthropogenic carbon is present in the actual data, I investigate how C* change in each water mass. Later, I will compare the results with the estimated uptake of C_{ant} for each water mass. These values are then compared with the annual increase in C*, normalised to 1994 and 2007, in order to evaluate the effect of the TSS based time normalisation of the data, and to the estimates of the C_{ant} increase determined with the eMLR(C*) method, $\Delta C_{ant}^{eMLR(C*)}$, presented in the previous chapter.

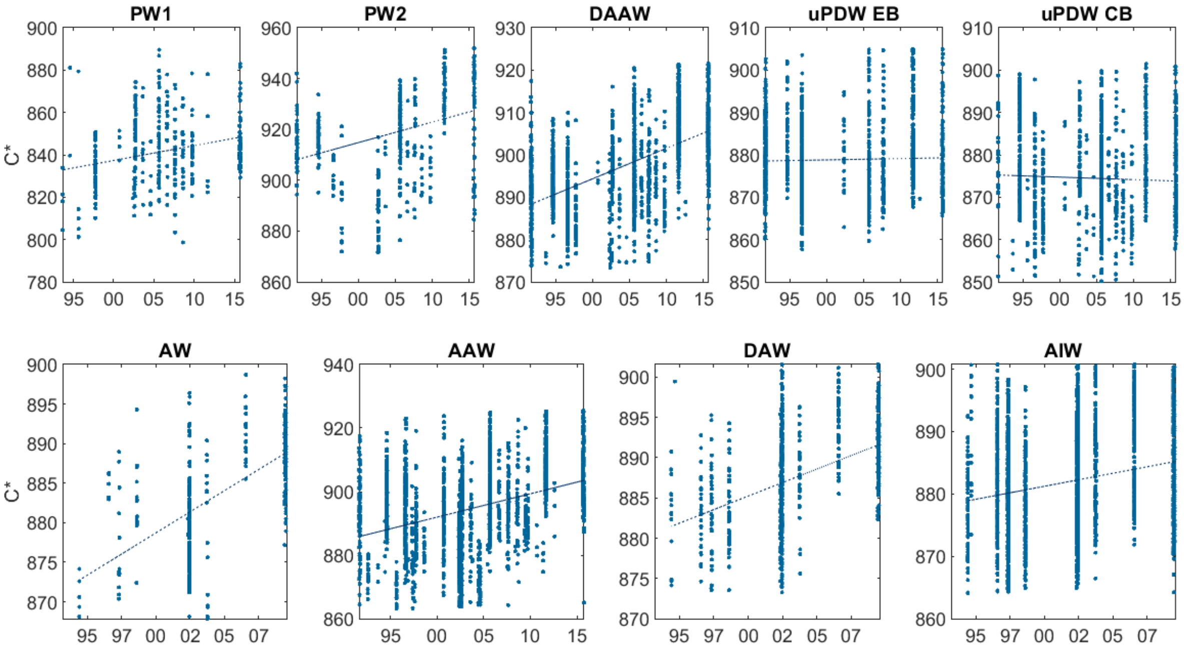

Figure 5.1: Increase in C* [μmol/kg] over time for each water mass. All data points outside two standard deviations are removed.

ΔC* is, as mentioned earlier, a result of both natural and anthropogenic contributions. If all assumptions (see Chapter 2) are true, then $\Delta C^*(t_2 - t_1)$ reflects the anthropogenic and natural gas exchange with the atmosphere:

$$\Delta C^{*}(t_2 - t_1) = \Delta C_{ant}(t_2 - t_1) + \Delta C_{nat}^{gasex}(t_2 - t_1). \tag{5.1}$$

$\Delta C_{nat}^{gasex}(t_2 - t_1)$ is in general smaller than ΔC_{ant} (Clement and Gruber, 2018). $\Delta C^{*}(t_2 - t_1)$ should therefore be comparable to $\Delta C_{ant}^{eMLR(C*)}$.

The evolution of C* over time in each water mass is shown in Figure 5.1. Table 5.1 presents the increase in C* based on the linear regressions, ΔC^{*}_{reg}, along with the difference in the adjusted C*, ΔC^{*}_{ref}, calculated by subtracting the mean value of C^{*}_{1994} from the mean value of C^{*}_{2007}. $\Delta C_{ant}^{eMLR(C*)}$ in Table 5.1 is the mean change in C_{ant} in each water mass based on the eMLR(C*) equations (Equation 3.11) used together with the GeoCap climatologies.

Table 5.1 and Figure 5.1 show that all water masses except for the uPDW EB/CB have an uptake of 10 ± 5 μmol/kg from 1994 to 2007 according to the regression analysis. An increase in the younger water masses (younger than ∼200 years) is expected since they have been in contact with the modern atmosphere. Similarly, I do not expect to see an increase in the deepest and oldest water masses of the Arctic Ocean.

Water Mass	$\Delta C_{ant}^{eMLR(C*)}$	ΔC^{*}_{reg}	ΔC^{*}_{ref}	Water Mass Age
PW1	-7.23 (-0.56)	11.31 (0.87)	8.08 (0.62)	1-5
PW2	16.80 (1.30)	10.92 (0.84)	8.30 (0.64)	1-5
AW	11.10 (0.85)	13.40 (1.03)	8.61 (0.66)	0 - ?
AAW	10.18 (0.78)	9.62 (0.74)	9.85 (0.76)	∼10
DAW	8.44 (0.65)	8.71 (0.67)	7.62 (0.59)	young
DAAW	8.37 (0.64)	9.36 (0.72)	10.68 (0.82)	∼20
AIW	5.03 (0.39)	5.46 (0.42)	5.43 (0.42)	ventilated each winter
uPDW EB	4.87 (0.38)	0.39 (0.03)	4.62 (0.36)	100-250
uPDW CB	4.44 (0.34)	-0.78 (-0.06)	1.75 (0.14)	100-450

Table 5.1: Table comparing ΔC_{ant}^{eMLR}, ΔC^{*}_{reg}, and ΔC^{*}_{ref} between 1994 and 2007, and water mass age. The values inside the parenthesis are the yearly uptake rate in μmol/kg yr. The water mass ages for the Arctic Ocean are taken from Figure 2 and 3 in Tanhua et al. (2009) (AAW and DAAW), from Rudels et al. (2012) (PW1 and PW2), and from Bluhm et al. (2015) (uPDW EB and uPDW CB). Tanhua et al. (2009) does not define water masses, but I compare the depth of my water masses with Figure 2 and 3. I could not find specific ventilation ages for DAW, but expect it to be relatively young, since it consists of AW which is heavily ventilated on its way north from lower latitudes (Anderson and Olsen, 2002). AIW is ventilated each winter in the Greenland Sea (Brakstad et al., 2019).

Table 5.1 shows that there are five water masses in that stand out with relatively large differences in the their $\Delta C_{ant}^{eMLR(C*)}$, ΔC^{*}_{reg}, and ΔC^{*}_{ref} values: PW1, PW2, AW, uPDW EB, and uPDW CB. If we assume constant stoichiometric ratios within a water mass, and well defined water mass definitions, the differences in the parameters can arise because of several reasons:

Firstly, the difference between ΔC^{*}_{reg} and ΔC^{*}_{ref} for each water mass gives information about the adequacy of the TSS-based adjustment of C* to the two reference years. Ideally, the trends should be similar, i.e. if the actual ocean behaves as assumed under TSS. Any difference between $\Delta C*_{reg}$ and $\Delta C*_{ref}$ can therefore be caused by errors in the TSS assumption. Secondly, depending on the spatial spreading of the data, errors in $\Delta C*_{reg}$ can arise from sampling bias. $\Delta C*_{ref}$ can adjust for the sampling bias to some extent, leading to differences in the two parameters. The calculation of C^*_{ref} helps to reduce effects of sampling bias since it adjusts all C* data points from 1991 to 2000, or 2001 to 2015, to one of the reference years, 1994 and 2007. Each water mass thus contains more data for each reference year, hopefully with a better spatial representation. Thirdly, differences in $\Delta C*_{ref}$ and ΔC_{ant}^{eMLR} can also arise from sampling bias, as the anthropogenic carbon estimates are determined for the full region of each water mass, while the $\Delta C*_{ref}$ estimates are based on the individual sampling locations - which differ between the eras. The eMLR(C*) equations can correct sampling bias since they are a product of ratios between predictor and response variables, and not an increase/decrease of $C*ref$ itself. Finally, the climatologies can have errors that affect $\Delta C_{ant}^{eMLR(C*)}$.

In this case, $\Delta C*_{reg}$ most likely has sampling bias for all water masses since the cruise data are spread so widely over time and space (see Figure 4.11). For example, there might be sampling bias in the DAAW data, since the uptake rate of $C_{ant}^{eMLR(C*)}$ in this water mass (0.64 μmol/kg yr) fits quite well with Ulfsbo et al. (2018). Ulfsbo et al. (2018) estimate the uptake rate of DAAW to be 0.56 ($\pm$0.15) for EB. The uptake rate calculated from $\Delta C*_{ref}$ for DAAW is higher than this, but the eMLR(C*) method might have adjusted for sampling bias in $\Delta C*_{ref}$, as explained above. For AW, I believe there are some problems with the TSS-assumption. The increase in the TSS normalized C*, $\Delta C*_{ref}$, is almost 5 μmol/kg lower than $\Delta C*_{reg}$. Studies on the C_{ant} saturation of the AW suggest that it has more ΔC_{ant} than expected from the atmospheric increase. Anderson and Olsen (2002) show this theoretically, while Skjelvan et al. (2008) based on data from the time series station Mike in the Norwegian Sea, find that the increase in carbon in the surface layer is larger than that expected from the atmospheric increase. These finding means there most likely are some errors in assuming a transient steady state in AW, since TSS assumes that the increase in ocean anthropogenic carbon tracks the atmosphere.

Both uPDW and EBDW/CBDW are included in the uPDW EB/uPDW CB as defined here. Most likely these have different rates of increase of C_{ant}. We expect very low or to undetectable rates of C_{ant} increase in the old and deep EBDW and CBDW, but some increase in the overlying uPDW. Ulfsbo et al. (2018) found an uptake rate of 0.46 μmol/kg·yr for uPDW in the Eurasian Basin. The uPDW can be found at depths from 700/800-1500/1600 meters. If we look at the uptake rate in this depth interval for uPDW EB/CB, we get 0.62 for EB and 0.74 for CB. Compared to Ulfsbo et al. (2018), this seem slightly high. The definition of uPDW EB/uPDW CB could be a problem if the stoichiometric ratios change between uPDW and EBDW/CBDW. However, from Figure 4.9, the water mass definition appears to be well defined for uPDW EB. For uPDW CB, on the other hand, the water masses do not seem to be as well defined because of the wider spread of data around the regression line. There are differences between $\Delta C*_{reg}$ and $\Delta C*_{ref}$ indicating problems with the TSS assumption for these water masses, especially in uPDW EB. Therefore, the main problem is probably found in the TSS assumption in uPDW EB since the water mass definition seems reasonable. While for uPDW CB, both the water mass definition and TSS assumption are problematic.

PW1 and PW2 are mixtures of many different water types close to the surface, which is not ideal for the eMLR(C*) method. The C* and AOU in the surface layer water masses can be affected by gas exchange. C* can therefore loose its conservative properties, and AOU become biased. This is probably the main reason for the differences between $C_{ant}^{eMLR(C*)}$ and $\Delta C*_{reg/ref}$ in these water masses.

5.2 Revelle factor

The Revelle factor equation, 2.7, can be used to estimate the potential uptake of C_{ant} in a water mass by rearranging the terms:

$$\Delta C_{ant}^{Rf} = \frac{DIC/\Delta pCO_2}{CO_2/Rf}, \tag{5.2}$$

where ΔC_{ant}^{Rf} is the "equilibrum increase", this is the increase expected for an ocean fully tracking the atmospheric increase in CO_2. DIC and CO_2 represent the mean concentration in the time period of interest, 1994 - 2007. ΔpC_2 is the atmospheric increase of pCO_2 in the same period, and Rf is the Revelle factor. Rf is calculated with the CO2SYS (Lewis and Wallace, 1998) for MATLAB (van Heuven et al., 2011). ΔC_{ant}^{Rf} can be compared to the ΔC_{ant}^{eMLR} estimates for the *youngest* water masses. However, some caution must be taken. In particular, the deep water masses are old and thus not expected to track the atmospheric CO_2 increase; here the equilibrium will be higher than the increase in C_{ant}. In addition, the equation assumes fully saturated water which is not the case in the Arctic Ocean and the Nordic seas (Tanhua et al., 2009; Olsen et al., 2010). For the AW, on the other hand, the equilibrium increase may be smaller than the estimated increase in C_{ant}, as it has been demonstrated that this can exceed what is expected from the increase in the atmosphere (Anderson and Olsen, 2002; Olsen et al., 2006; Skjelvan et al., 2008).

The equilibrium increase calculated from Equation 5.2 and presented in Table 5.2 was calculated from the data used to make the eMLR(C*) equations, while the ΔC_{ant}^{eMLR} estimates are based on the climatologies. Ideally, the equilibrium increase should also have been calculated using the climatologies, but unfortunately I did not make climatologies for total carbon which is needed in the CO2SYS package in MATLAB to calculate the Revelle factor. Therefore some of the differences may be due to spatial biases in the data.

Water mass	PW1	PW2	AW	AAW	DAW	DAAW	AIW	uPDW EB	uPDW CB
Uptake potential	5.36	8.68	10.92	10.18	11.0	10.34	11.32	11.35	11.71
ΔC_{ant}^{eMLR}	-7.23	16.80	11.10	10.18	8.44	8.37	5.03	4.87	4.44

Table 5.2

Table 5.2 shows the calculated equilibrium increase compared to the estimates of $\Delta C_{ant}^{eMLR(C*)}$. The equilibrium increase for AW is lower than ΔC_{reg}, just like ΔC_{ref} and ΔC_{ant}^{eMLR} in Table 5.1. As mentioned above, this aligns with previous findings in the Nordic seas since the increase in C_{ant} in the AW was higher than expected from the atmosphere in the time period considered (Olsen et al., 2006; Skjelvan et al., 2008).

For PW1 and PW2, ΔC_{ant}^{Rf} and $\Delta C_{ant}^{eMLR(C*)}$ are very different. Here, this is likely a result of errors in the $\Delta C_{ant}^{eMLR(C*)}$ estimates, as discussed above. ΔC_{ant}^{Rf} for these two water masses seems more reasonable and they are closer to $\Delta C*_{reg}$ in Table 5.1.

The older water masses are overestimated in ΔC_{ant} because of the underlying assumptions in the Revelle factor. There is no point in comparing them to ΔC_{ant}^{Rf} other than checking that the estimates of ΔC_{ant}^{eMLR} are not higher.

5.3 Denitrification

Errors in the $\Delta C_{ant}^{eMLR(C*)}$ estimates can arise from *denitrification*, since this process changes the underlying relationship between predictor (nitrate) and estimator(C*) in the water masses. If this process happens during the period of interest it is especially bad for the $\Delta C_{ant}^{eMLR(C*)}$ estimates, since the change will be misinterpreted as a change in C_{ant}. Denitrification can happen when there is no oxygen in the water mass and anaerobic bacteria reduce nitrate in the process of breaking down organic material. Nitrate is reduced several times and ultimately escapes the water mass as N_2. If nitrate is included in the eMLR(C*) equations, the denitrification affects the estimates of ΔC_{ant}. However, denitrification is expected to reduce the quality (increse the RMSE value) in the eMLR(C*) equations and nitrate will therefore most likely not be favoured in the variable selection process described in Section 3.2.3.

Figure 5.2 relates phosphate to nitrate for all nine water masses. The Redfield ratio used in this thesis has a ratio of 17.5:1 for nitrate vs. phosphate. The grey dotted lines in Figure 5.2 represent this ratio and compare it to the nitrate-phosphate relationships in each water mass. Whenever the data lie below this line, it is a sign of denitrification.

PW1 and PW2 show signs of denitrification in Figure 5.2. However, nitrate is only selected 4/10 times in the ten best eMLR(C*) equations which is the least times a variable was selected for PW1. It seems like nitrate is reducing the quality in the equations, as described above. In this way, the eMLR(C*) method seems to remove the effects of denitrification to some degree. On the other hand, nitrate is selected 7/10 in PW2 even though this water mass has clear signs of denitrification. There is also indication of denitrification in AAW and DAAW. However, nitrate is selected 8/10 times in AAW, but only 4 times in DAAW. The rest of the water masses seem to follow the expected stoichiometric ratios. uPDW EB and uPDW CB is combined in Figure 5.2, but I also looked at them individually and there are no signs of denitrification in either one of them.

For future work, we can try removing nitrate from the predictor variables in the water masses with denitrification to potentially improve the eMLR(C*) equations.

5.4 Anthropogenic CO_2

5.4.1 Nordic seas

The C_{ant} uptake in the Nordic seas agrees well with previous studies and expectations. Also, there is good agreement in uptake across the boundaries between the different water masses all over the Nordic seas, i.e where different sets of eMLR(C*) equations have been used. This is a sign of well

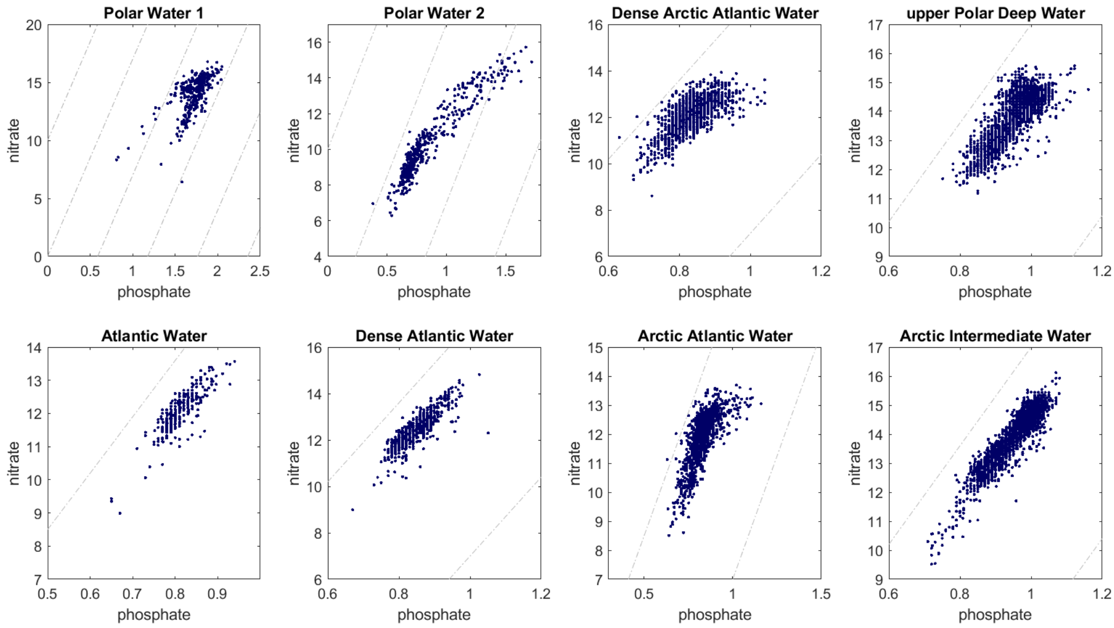

Figure 5.2: Nitrate vs. phosphate for all water masses. The dashed lines are the expected stoichiometric relationships between nitrate and phosphate (17.5:1) when there is no denitrification.

defined water masses. The C_{ant} increase in the AW is, however, potentially underestimated since the TSS assumption used to normalise the data to 1994 and 2007, is unsuited for this water mass. The estimates of ΔC_{ant} in the Greenland Sea are lower and more homogeneous throughout the water column than found by Olsen et al. (2006). The recent increase of deep mixing in the Greenland Sea gyre might explain this. The winter mixed layer depth has gradually increased since 2003, with a maximum depth of 1500 meters during the winter of 2011 (Brakstad et al., 2019). The deepening ventilation brings newly formed water down, but also older water up towards the surface. The young water is rich in C_{ant}, while the old water from below is not. Therefore, the upward mixing of older water might slow the increase of ΔC_{ant} in the water column all the way up to the surface. Deep mixed layers in the Irminger Sea, on the other hand, are fully saturated in C_{ant} (Fröb et al., 2019). This difference suggest that the interaction between deep mixing and C_{ant} uptake may be different in the Greenland and Irminger Sea. Consequently, this would be an interesting topic for future studies.

The mixed layer depth is not the only thing that has changed in the Greenland Sea. The water masses are becoming warmer, saltier, and lighter (Lauvset et al., 2018; Brakstad et al., 2019). There has also been a shift in water masses in the deeper parts of the basin. Before 2002, the Greenland Sea Deep Water (GSDW), a water mass denser than AIW, was present in the Greenland Sea. But the presence of GSDW gradually decreases from 1990 to 2002, when it almost vanishes completely. From 1994 to 2002 it is only present below 1500 meters. The climatologies are not able to describe the changing water masses, in addition to the eMLR(C*) equations not being suited for changes in water mass distribution. This can lead to errors in the results since the climatologies are based on data from 1985 to present, and might be part of the reason why the uptake is different from previous studies.

5.4.2 Arctic Ocean

The uptake of C_{ant} in AAW and DAAW in the Arctic Ocean resembles previous estimates, as described in Results. AAW and DAAW are the best defined water masses in the Arctic Ocean based on all the results so far, but they do show signs of denitrification and might have errors because of this. In Figure 4.9, PW2, AAW, and DAAW have scatter on the lower end of the scale, indicating poor water mass definition. Since these three water masses also show signs of denitrification, this is most likely the reason for the scatter in Figure 4.9.

PW1 also shows signs of denitrification, but there are not much scatter in Figure 4.9. This may simply come from the fact that there is very little data for PW1, but if we look at Table 4.1, PW1 only uses nitrate in 4/10 equations and might therefore not be affected too much by denitrification, as discussed above. Overall, Table 4.1 shows that nitrate is the variable least used in all of the equations.

DAAW is modified Atlantic Water and is younger than the uPDW. Therefore, we would expect a larger C_{ant} increase in this water mass. However, DAAW is also affected by denitrification and might have errors. Either way, the uptake in uPDW EB/CB seems suspiciously high compared to DAAW and the other water masses above, and the sudden increase in uPDW EB/CB at 800 meters is probably due to errors in the water mass definition. I was not able to detect any deep water in the Eurasian or Canadian Basin. Ulfsbo et al. (2018) define both uPDW and EBDW/CBDW according to Rudels et al. (2012). I divide uPDW into uPDW CB/EB in lack of finding any deep water, even though Ulfsbo et al. (2018) used the same water mass definition as I have done. We might expect some uptake deep in the Eurasian Basin because of the dense water flowing through St. Anna Trough from the Barents Sea. However, the deepest reaching convection and it's properties within the Arctic Ocean is not yet described (Rudels et al., 2012).

The Arctic Ocean has gone through changes during the study period. One of the assumptions behind the eMLR(C*) method is that the underlying properties of the water masses remain the same. We know that there has been an increase in both temperature and salinity in AW entering the Arctic Ocean, especially in the upper 250 meters (Lind et al., 2018). Since temperature and salinity are important variables and used in almost all selected MLR equations, these changes are most likely affecting the results together with the other errors sources mentioned earlier. In addition, the climatologies are not able to describe changes since they represent mean state based on data gathered between 1985 and present. Errors can arise from this as well. I suspect the uptake of C_{ant} between 100-250 meters in PW1, PW2 and AAW are affected by the changes described by Lind et al. (2018), together with the other errors mentioned earlier.

One could imagine that the recent summer sea ice loss, leading to longer freeze-up seasons and more brine rejection (Onarheim et al., 2018), increasing areas with open water, and "atlantification" of the Barents Sea and Eurasian Basin (Lind et al., 2018; Polyakov et al., 2017) would lead to large uptake of C_{ant} in the surface layer in these areas. However, as these processes are mostly happening in surface near layers, there are many sources of error and the eMLR(C*)-method is not well suited. Any increase may be hidden in the uncertainties. Also, the largest increase in brine production due to less summer sea ice and longer freeze-up season happens along the continental slopes in the Arctic Ocean (Onarheim et al., 2018). We would therefore expect that significant ventilation in these areas would lead to an uptake pattern similar to figure 6a in Tanhua et al., 2009, but the results do not look like this.

5.4.3 Inventory

The estimated column inventories of ΔC_{ant} in the Nordic seas (Figure 4.12) looks very similar to that of Figure 5 in Olsen et al. (2010), except that they find the highest inventories in the Greenland Sea. The estimated column inventories in Figure 4.12 is about 31% of their Figure 5 at the place with the highest inventory in the Lofoten Basin, about 24% in the Norwegian Sea, and 23% in the Greenland Sea. The total atmospheric increase from preindustrial times to 2002, the time period evaluated by Olsen et al. (2010), was 93.3 ppm, and the increase from 1994 to 2007 25 ppm. I.e. the increase of atmospheric CO_{ant} in the study period is 27 % of the total increase since preindustrial times. Thus, assuming that the inventory of the oceans follows the atmospheric content of CO_2, my inventory estimate for the Nordic seas is in full accordance with the literature.

The highest column inventories of ΔC_{ant} in the Nordic seas and Arctic Ocean are found in the Eurasian Basin, as seen from Figure 4.14. I did not expect to find the highest column inventories of ΔC_{ant} in the Arctic Ocean, since the advected C_{ant} through the Barents Sea and Fram Strait is expected to be the main source of C_{ant} here. High increase in PW2 and uPDW EB/CB are the main contributors to the inventory. However, as the increase in C_{ant} is probably overestimated for these water masses, as discussed above, the column inventories for the Arctic Ocean is probably also overestimated. Brine rejection could contribute to additional uptake in the Arctic Ocean, but the volume and uptake potential of C_{ant} in brine is not fully understood and are most likely small compared to the C_{ant} advected into AO (Smedsrud et al., 2013).

5.4.4 Comments on water mass definitions

A big difference between the Nordic seas and the Arctic Ocean is how well the estimated uptake match at the borders between water masses. In the Nordic seas, the water masses seem well defined since there are no sharp gradients in the estimated C_{ant} increase at the borders. In the Arctic Ocean, on the other hand, the gradients are unrealistically sharp in the surface near water masses and between uPDW EB/CB and DAAW, indicating bad water mass definitions. This is expected since I could not identify any CBDW or EBDW. The results also vary a lot in the upper 200 meters depending on how much surface water I exclude from the eMLR(C*) equations. This is not the case for the Nordic seas where ΔC_{ant} changed very little (1 - 2 μmol/kg) when I varied the depth of the excluded surface water. The conditions in the Arctic Ocean are more complicated than in the Nordic seas because of sea ice, brine rejection, and fresh water input. This especially has an effect on the water masses near the surface. The gradients between AAW and DAAW seem OK, which means that these water masses are better defined.

Chapter 6

Conclusions

The eMLR(C*) method is suited for some water masses, but for others it needs more work. The method seems to work well for the Nordic seas, except that it appears to underestimate the increase in the Atlantic Water because of errors assuming TSS in this water mass (Anderson and Olsen, 2002). The estimates of C_{ant} uptake and inventory fit quite well with expectations and previous studies. Also, the gradients across different water masses look natural. The biggest deviance from my immediate expectations is found in the Greenland Sea, where my estimates are lower than the results of Olsen et al. (2006) and Olsen et al. (2010). However, the results seem logical when we compare them to the changes in mixed layer depth (Brakstad et al., 2019).

The uptake and inventory estimates in the Arctic Ocean appear too high compared to the Nordic seas, especially if the main contributor of C$_{ant}$ is the inflowing Atlantic Water, and not the local processes. The uptake in PW2 and uPDW EB/CB are much higher than expected, and make up a significant amount of the total inventory between 1994 and 2007. In PW2, AAW, and DAAW there are problems with denitrification. There are, in general, large uncertainties in PW1 and PW2 since their definition does not suit the eMLR(C*) method. uPDW EB/CB also suffer from unsuited water mass definitions since the old deep water of both basins are added to uPDW, but there are also problems with the TSS assumption in these water masses. Even though Figure 4.9 has little scatter for uPDW EB, the eMLR(C*) method is very sensitive to how the water masses are defined. Other water mass definition schemes should be explored in future studies. In summary, the estimates for all water masses of the Arctic Ocean have errors. The eMLR(C*) method is therefore, so far, not well suited here.

There are in general little data, especially in the Arctic Ocean. The region is under-sampled when it comes to both time and space, which affects the accuracy of the different steps in the eMLR(C*) method. There are many sources of error in the estimates because of all these steps, all with their own assumptions. I was unfortunately not able to estimate uncertainties because of too little time and the complexity of the Monte Carlo method that would be needed. Clement and Gruber (2018) estimated an uncertainty of ±20% in the North Atlantic, and I believe the Nordic seas have a similar uncertainty. The values is most likely higher for the Arctic Ocean. If I had more data, I could test the equations on different data sets to see how well they correspond. This would be a big advantage, and lead to more robust results.

6.1 Future work

There is much to explore and improve in the method used in this thesis. Only selecting equations based on the RMSE values is maybe not the best solution when considering the Nordic seas and the Arctic Ocean. An idea could be to review plots of C^*_{pred} vs. C^*_{obs}, similar to Figure 4.9, more thoroughly, and choose the equations with the best fits, such as Equation 8 and 9 in Figure 4.10. In this figure, 8/10 equations for AIW have scatter above the ideal linear relationship, indicating that some parts of this water mass are not well described. However, Equation 8 and 9 do not have this at all, and are therefore better fitted to the water mass. These two equations are the only ones that have salinity as a predictor variable. Because of this, it looks like salinity is needed to account for mixing in this water mass, even though the RMSEs of other equations without salt are higher.

The water mass definitions of Rudels et al. (2012) are created for physical oceanographic purposes, and might not be the best way to divide the water masses. The definition of PW1 and PW2 are especially problematic since they include different types of water. For future work, it would be an idea to try another water mass definition since this seems to be one of the most sensitive aspects. I experienced this myself when I tried different intervals of excluded surface water. Additionally, the climatologies need to be improved further. These contain some outliers that should have been be removed, and we can look for more data to include in the gridding.

Bibliography

Anderson, L. G. and Olsen, A. (2002). Air-sea flux of anthropogenic carbon dioxide in the North Atlantic. *Geophysical Research Letters*, 29(17):16–1–16–4.

Anderson, L. G., Ulfsbo, A., Ericson, Y., and Schauer, U. (2011). Seawater carbonate chemistry in the Arctic Ocean during POLARSTERN cruise ARK-XXVI/3 (TransArc), in August - October, 2011.

Behrendt, A., Sumata, H., Rabe, B., and Schauer, U. (2018). Udash – unified database for arctic and subarctic hydrography. *Earth System Science Data*, 10(2):1119–1138.

Bluhm, B. A., Kosobokova, K. N., and Carmack, E. C. (2015). A tale of two basins: An integrated physical and biological perspective of the deep Arctic Ocean. *Progress in Oceanography*, 139:89–121.

Bosse, A., Fer, I., Søiland, H., and Rossby, T. (2018). Atlantic Water Transformation Along Its Poleward Pathway Across the Nordic Seas. *Journal of Geophysical Research: Oceans*, 123(9):6428–6448.

Brakstad, A., Våge, K., Håvik, L., and Moore, G. W. K. (2019). Water Mass Transformation in the Greenland Sea during the Period 19862016. *Journal of Physical Oceanography*, 49(1):121–140.

Carter, B. R., Feely, R. A., Mecking, S., Cross, J. N., Macdonald, A. M., Siedlecki, S. A., Talley, L. D., Sabine, C. L., Millero, F. J., Swift, J. H., Dickson, A. G., and Rodgers, K. B. (2017). Two decades of Pacific anthropogenic carbon storage and ocean acidification along Global Ocean Ship-based Hydrographic Investigations Program sections P16 and P02. *Global Biogeochemical Cycles*, 31(2):306–327.

Clement, D. and Gruber, N. (2018). The eMLR(C*) Method to Determine Decadal Changes in the Global Ocean Storage of Anthropogenic CO2. *Global Biogeochemical Cycles*, 32(4):654–679.

Egleston, E. S., Sabine, C. L., and Morel, F. M. (2010). Revelle revisited: Buffer factors that quantify the response of ocean chemistry to changes in DIC and alkalinity. *Global Biogeochemical Cycles*, 24(1):1–9.

Eldevik, T., Nilsen, J. E., Iovino, D., Anders Olsson, K., Sandø, A. B., and Drange, H. (2009). Observed sources and variability of Nordic seasoverflow. *Nature Geoscience*, 2(6):406–410.

Friedlingstein, P., Cox, P., Betts, R., Bopp, L., von Bloh, W., Brovkin, V., Cadule, P., Doney, S., Eby, M., Fung, I., Bala, G., John, J., Jones, C., Joos, F., Kato, T., Kawamiya, M., Knorr, W., Lindsay, K., Matthews, H. D., Raddatz, T., Rayner, P., Reick, C., Roeckner, E., Schnitzler, K.-G., Schnur, R., Strassmann, K., Weaver, A. J., Yoshikawa, C., and Zeng, N. (2006). Climatecarbon cycle feedback analysis: Results from the c4mip model intercomparison. *Journal of Climate*, 19(14):3337–3353.

Friis, K., Körtzinger, A., Pätsch, J., and Wallace, D. W. (2005). On the temporal increase of anthropogenic CO2in the subpolar North Atlantic. *Deep-Sea Research Part I: Oceanographic Research Papers*, 52(5):681–698.

Fröb, F., Olsen, A., Becker, M., Chafik, L., Johannessen, T., Reverdin, G., and Omar, A. (2019). Wintertime CO_2 Variability in the Subpolar North Atlantic Since 2004. *Geophysical Research Letters*, 46(3):1580–1590.

Garcia, H. E. and Gordon, L. I. (1992). Oxygen solubility in seawater: Better fitting equations. *Limnology and Oceanography*, 37(6):1307–1312.

Gruber, N., Clement, D., Carter, B. R., Feely, R. A., Van Heuven, S., Hoppema, M., Ishii, M., Key, R. M., Kozyr, A., Lauvset, S., Le Monaco, C., T, M. J., Murata, A., Olsen, A., Perez, F. F., Abine, C. L., Tanhua, T., and Wanninkhof, R. (2018). The oceanic sink for anthropogenic CO2 from 1994 to 2007. *Science*, (submitted).

Gruber, N., Keeling, C. D., Bacastow, R. B., Guenther, P. R., Lueker, T. J., Wahlen, M., Meijer, H. A., Mook, W. G., and Stocker, T. F. (1999). Spatiotemporal patterns of carbon-13 in the global surface oceans and the oceanic Suess effect. *Global Biogeochemical Cycles*, 13(2):307–335.

Gruber, N. and Sarmiento, J. L. (2002). *Chapter 9 . LARGE-SCALE BIOGEOCHEMICAL PHYSICAL INTERACTIONS IN ELEMENTAL CYCLES*, volume 12.

Gruber, N., Sarmiento, J. L. S., and F, T. (1996). An improved method for detecting anthropogenic CO$_2$ in the oceans. *Global Biogeochemical Cycles*, 10(4):809–837.

Jeansson, E., Olsen, A., Eldevik, T., Skjelvan, I., Omar, A. M., Lauvset, S. K., Nilsen, J. E. Ø., Bellerby, R. G., Johannessen, T., and Falck, E. (2011). The Nordic Seas carbon budget: Sources, sinks, and uncertainties. *Global Biogeochemical Cycles.*

Jones, E. M. and Ulfsbo, A. (2017). Seawater carbonate chemistry measured on water bottle samples during POLARSTERN curise PS94 (ARK-XXIX/3).

Key, R. M., Kozyr, A., Sabine, C. L., Lee, K., Wanninkhof, R., Bullister, J. L., Feely, R. A., Millero, F. J., Mordy, C., and Peng, T. H. (2004). A global ocean carbon climatology: Results from Global Data Analysis Project (GLODAP). *Global Biogeochemical Cycles*, 18(4):1–23.

Khatiwala, S., Tanhua, T., Mikaloff Fletcher, S., Gerber, M., Doney, S. C., Graven, H. D., Gruber, N., McKinley, G. A., Murata, A., Ríos, A. F., and Sabine, C. L. (2013). Global ocean storage of anthropogenic carbon. *Biogeosciences*, 10(4):2169–2191.

Körtzinger, A., Hedges, J. I., and Quay, P. D. (2001). Redfield ratios revisited: Removing the biasing effect of anthropogenic CO2. *Limnology and Oceanography*, 46(4):964–970.

Lauvset, S. K., Brakstad, A., Våge, K., Olsen, A., Jeansson, E., and Mork, K. A. (2018). Continued warming, salinification and oxygenation of the Greenland Sea gyre. *Tellus, Series A: Dynamic Meteorology and Oceanography*, 70(1):1–9.

Lauvset, S. K., Key, R. M., Olsen, A., van Heuven, S., Velo, A., Lin, X., Schirnick, C., Kozyr, A., Tanhua, T., Hoppema, M., Jutterström, S., Steinfeldt, R., Jeansson, E., Ishii, M., Perez, F. F., Suzuki, T., and Watelet, S. (2016). A new global interior ocean mapped climatology: the 1 × 1 glodap version 2. *Earth System Science Data*, 8:325–340.

Le Quéré, C., Andrew, R. M., Friedlingstein, P., Sitch, S., Pongratz, J., Manning, A. C., Korsbakken, J. I., Peters, G. P., Canadell, J. G., Jackson, R. B., Boden, T. A., Tans, P. P., Andrews, O. D., Arora, V. K., Bakker, D. C. E., Van Der Laan-Luijkx, I. T., Van Der Werf, G. R., Van Heuven, S., Viovy, N., Vuichard, N., Walker, A. P., Watson, A. J., Wiltshire, A. J., Zaehle, S., and Zhu, D. (2018). Global Carbon Budget 2017. *Earth Syst. Sci. Data Etsushi Kato Markus Kautz Ralph F. Keeling Kees Klein Goldewijk Nathalie Lefèvre Andrew Lenton Danica Lombardozzi Nicolas Metzl Yukihiro Nojiri Antonio Padin Janet Reimer*, 1010333739(10):405–448.

Lewis, E. and Wallace, D. (1998). Program developed for CO2 system calculations. ORNL/CDIAC-105.

Lind, S., Ingvaldsen, R. B., and Furevik, T. (2018). Arctic warming hotspot in the northern Barents Sea linked to declining sea-ice import. *Nature Climate Change*, 8(7):634–639.

Maier-Reimer, E. and Hasselmann, K. (1987). Transport and storage of co2 in the ocean - an inorganic ocean-circulation carbon cycle model. *Climate Dynamics*, 2(2):63–90.

Martiny, A. C., Vrugt, J. A., Primeau, F. W., and Lomas, M. W. (2013). Regional variation in the particulate organic carbon to nitrogen ratio in the surface ocean. *Global Biogeochemical Cycles*, 27(3):723–731.

Mauritzen, C. (1996). Production of dense overflow waters feeding the North Atlantic across the Greenland-Scotland Ridge. Part 2: An inverse model. *Deep-Sea Research Part I: Oceanographic Research Papers*, 43(6):807–809.

Olsen, A., Key, R. M., van Heuven, S., Lauvset, S. K., Velo, A., Lin, X., Schirnick, C., Kozyr, A., Tanhua, T., Hoppema, M., Jutterstrm, S., Steinfeldt, R., Jeansson, E., Ishii, M., Prez, F. F., and Suzuki, T. (2016). The global ocean data analysis project version 2 (glodapv2) an internally consistent data product for the world ocean. *Earth System Science Data (Online)*, 8(2).

Olsen, A., Omar, A. M., Bellerby, R. G., Johannessen, T., Ninnemann, U., Brown, K. R., Olsson, K. A., Olafsson, J., Nondal, G., Kivimäe, C., Kringstad, S., Neill, C., and Olafsdottir, S. (2006). Magnitude and origin of the anthropogenic CO2increase and13C Suess effect in the Nordic seas since 1981. *Global Biogeochemical Cycles*, 20(3).

Olsen, A., Omar, A. M., Jeansson, E., Anderson, L. G., and Bellerby, R. G. J. (2010). Nordic seas transit time distributions and anthropogenic CO<subscr>2</subscr>. *J. Geophys. Res*, 115.

Onarheim, I. H., Eldevik, T., Smedsrud, L. H., and Stroeve, J. C. (2018). Seasonal and regional manifestation of Arctic sea ice loss. *Journal of Climate*, 31(12):4917–4932.

Polarforskningssekretariatet (2017). Lomonosov Ridge off Greenland (LOMROG) - Meteorological, Oceanographic and Ship Data Collected Onboard Icebreaker Oden during August 12 through September 19 2007. *Svensk nationell datatjänst. Version 1.0.*

Polyakov, I. V., Pnyushkov, A. V., Alkire, M. B., Ashik, I. M., Baumann, T. M., Carmack, E. C., Goszczko, I., Guthrie, J., Ivanov, V. V., Kanzow, T., Krishfield, R., Kwok, R., Sundfjord, A., Morison, J., Rember, R., and Yulin, A. (2017). Greater role for Atlantic inflows on sea-ice loss in the Eurasian Basin of the Arctic Ocean. *Science*, 356(6335):285–291.

Redfield, A. C., Ketchum, B. H., and Richards, F. A. (1963). The influence of organisms on the composition of sea-water. In Hill, M. N., editor, *The sea: ideas and observations on progress in the study of the seas*, volume 2, pages 26–77. Interscience, New York.

Rudels, B., Anderson, L., Eriksson, P., Fahrbach, E., Jakobsson, M., Jones, E., Melling, H., Prinsenberg, S., Schauer, U., and Yao, T. (2012). Observations in the ocean. In Lempke, P. and Jacobi, H. W., editors, *Arctic Climate Change: The ACSYS Decade and Beyond*, chapter 4. Springer Science+Business Media B.V.

Sabine, C. L., Feely, R. A., Gruber, N., Key, R. M., Lee, K., Bullister, J. L., Wanninkhof, R., Wong, C. S., Wallace, D. W. R., Tilbrook, B., Millero, F. J., Peng, T.-H., Kozyr, A., Ono, T., and Rios, A. F. (2004). The Oceanic Sink for Anthopogenic {CO_2}. *Science*.

Sarmiento, J. L. and Gruber, N. (2006). *Ocean Biogeochemical Dynamics*. Princeton University Press.

Sarmiento, J. L., Orr, J. C., and Siegenthaler, U. (1992). A perturbation simulation of CO2 uptake in an ocean general circulation model. *Journal of Geophysical Research*, 97(C3):3621–3645.

Schwinger, J., Tjiputra, J. F., Heinze, C., Bopp, L., Christian, J. R., Gehlen, M., Ilyina, T., Jones, C. D., Salas-Mlia, D., Segschneider, J., Sfrian, R., and Totterdell, I. (2014). Nonlinearity of ocean carbon cycle feedbacks in cmip5 earth system models. *Journal of Climate*, 27(11):3869–3888.

Skjelvan, I., Falck, E., Rey, F., and Kringstad, S. B. (2008). Inorganic carbon time series at Ocean Weather Station M in the Norwegian Sea. *Biogeosciences*, 5(2):549–560.

Smedsrud, L. H., Esau, I., Ingvaldsen, R. B., Eldevik, T., Haugan, P. M., Li, C., Lien, V. S., Olsen, A., Omar, A. M., Risebrobakken, B., Sandø, A. B., Semenov, V. A., and Sorokina, S. A. (2013). The role of the Barents Sea in the Arctic climate system. *Reviews of Geophysics*, 51(3):415–449.

Talley, L., Feely, R., Sloyan, B., Wanninkhof, R., Baringer, M., Bullister, J., Carlson, C., Doney, S., Fine, R., Firing, E., Gruber, N., Hansell, D., Ishii, M., Johnson, G., Katsumata, K., Key, R., Kramp, M., Langdon, C., Macdonald, A., Mathis, J., McDonagh, E., Mecking, S., Millero, F., Mordy, C., Nakano, T., Sabine, C., Smethie, W., Swift, J., Tanhua, T., Thurnherr, A., Warner, M., and Zhang, J.-Z. (2016). Changes in ocean heat, carbon content, and ventilation: A review of the first decade of go-ship global repeat hydrography. *Annual Review of Marine Science*, 8(1):185–215. PMID: 26515811.

Tanhua, T., Jones, E. P., Jeansson, E., Jutterström, S., Smethie, W. M., Wallace, D. W., and Anderson, L. G. (2009). Ventilation of the arctic ocean: Mean ages and inventories of anthropogenic CO2 and CFC-11. *Journal of Geophysical Research: Oceans*, 114(1):1–11.

Tanhua, T., Kortzinger, A., Friis, K., Waugh, D. W., and Wallace, D. W. R. (2007). An estimate of anthropogenic CO2 inventory from decadal changes in oceanic carbon content. *Proceedings of the National Academy of Sciences*, 104(9):3037–3042.

Ulfsbo, A., Jones, E. M., Casacuberta, N., Korhonen, M., Rabe, B., Karcher, M., and van Heuven, S. M. (2018). Rapid Changes in Anthropogenic Carbon Storage and Ocean Acidification in the Intermediate Layers of the Eurasian Arctic Ocean: 19962015. *Global Biogeochemical Cycles*.

van Heuven, S., Pierrot, D., Rae, J. W. B., Lewis, E., and Wallace, D. W. R. (2011). MATLAB program developed for CO2 system calculationse. *ORNL/CDIAC-105b, Carbon Dioxide Information Analysis Center, Oak Ridge National Laboratory, US Department of Energy, Oak Ridge, Tennessee.*

Walczowski, W. (2013). Frontal structures in the West Spitsbergen current margins. *Ocean Science*, 9(6):957–975.

Wallace, D. W. R. (1995). *Monitoring global ocean carbon inventories.* Ocean Observing System Development, College Station, Texas.

W.R.Wallace, D. (2001). Chapter 6.3 storage and transport of excess co2 in the oceans:the jgofs/woce global co2 survey. In Siedler, G., Church, J., and Gould, J., editors, *Ocean Circulation and Climate*, volume 77 of *International Geophysics*, pages 489 – L. Academic Press.

Yamamoto-Kawai, M., McLaughlin, F. A., Carmack, E. C., Nishino, S., Shimada, K., and Kurita, N. (2009). Surface freshening of the Canada Basin, 2003-2007: River runoff versus sea ice meltwater. *Journal of Geophysical Research: Oceans*, 114(4):2003–2007.